Evaluating the impact of spatial resolution on tropospheric NO₂ column comparisons within urban areas using high-resolution airborne data

Laura M. Judd[1,2], Jassim A. Al-Saadi[1], Scott J. Janz[3], Matthew G. Kowalewski[3,4], R. Bradley Pierce[5], James J. Szykman[6],
Lukas C. Valin[6], Robert Swap[3], Alexander Cede[7], Moritz Mueller[7,8], Martin Tiefengraber[7,8], Nader Abuhassan[3,9], David Williams[6]

[1]NASA Langley Research Center, Hampton, VA, 23681, United States
[2]NASA Postdoctoral Program, Hampton, VA, 23681, United States
[3]NASA Goddard Space Flight Center, Greenbelt, MD, 20771, United States
[4]Universities Space Research Association, Columbia, MD, 21046, United States
[5]University of Wisconsin-Madison Space Science and Engineering Center, Madison, WI, 53706, United States
[6]United States Environmental Protection Agency Office of Research and Development, Triangle Research Park, NC, 27709, United States
[7]LuftBlick, Kreith, Austria
[8]Department of Atmospheric and Cryospheric Science, University of Innsbruck, Innsbruck, Austria
[9]Joint Center for Earth Systems Technology, University of Maryland-Baltimore County, Baltimore, MD, 21228, United States

Correspondence to: Laura M. Judd (laura.m.judd@nasa.gov)

Abstract. NASA deployed an airborne UV/Visible spectrometer, GeoTASO, in May-June 2017 to produce high resolution (approximately 250 × 250 m), gapless NO₂ datasets over the western shore of Lake Michigan and over the Los Angeles Basin. Results show that the airborne tropospheric vertical column retrievals compare well with ground-based Pandora spectrometer column NO₂ observations (r²=0.91 and slope of 1.03). Apparent disagreements between the two measurements can be sensitive to the coincidence criteria and are often associated with large local variability, including rapid temporal changes and also spatial heterogeneity that may be observed differently by the sunward viewing Pandora observations. The gapless mapping strategy executed during the 2017 GeoTASO flights provides data suitable for averaging to coarser areal resolutions to simulate satellite retrievals. As simulated satellite pixel area increases to values typical of TEMPO, TROPOMI, and OMI, the agreement with Pandora measurements is degraded as localized polluted plumes observed by Pandora are spatially averaged over larger areas (aircraft-to-Pandora slope: TEMPO scale=0.88; TROPOMI scale=0.77; OMI scale=0.57). This behavior suggests that satellite products are representative of individual Pandora observations up to a certain pollution scale that depends on satellite spatial resolution. In these two regions, Pandora and TEMPO or TROPOMI have the potential to compare well up to pollution scales of 30x10¹⁵ molecules cm⁻². Two publicly available OMI tropospheric NO₂ retrievals are both found to be biased low with respect to Pandora observations (NASA V3 Standard Product slope = 0.18 and Berkeley High Resolution Product slope=0.30). However, the agreement improves when higher resolution a priori inputs are used for the tropospheric air mass factor calculation. Overall, this work explores best practices for satellite validation strategies by showing the sensitivity to product spatial resolution and demonstrates how the high spatial resolution NO₂ data retrieved from airborne spectrometers, such as GeoTASO, can be used with high temporal resolution surface observations to evaluate the influence of spatial heterogeneity on validation results.

1 Introduction

Nitrogen oxides (NOₓ: NO + NO₂) are primarily emitted via fossil fuel combustion, soil microbial processes, biomass burning and lightning. NO₂ is an important precursor of ozone and particulate matter, making it one of the six criteria air pollutants monitored by the United States Environmental Protection Agency (EPA: https://www.epa.gov/criteria-air-

pollutants). Unlike less reactive trace gases having atmospheric lifetimes of days or longer, the atmospheric lifetime of NO_x is reported to be on the order of hours in the daytime polluted boundary layer (Liang et al. 1998; Beirle et al., 2011; Liu et al., 2016). This short lifetime along with large variations in emission rates from sources causes the spatial distribution of NO_2 in polluted regions to be highly heterogeneous, making it difficult to characterize over urban areas without high
5   spatiotemporal observations.

     Since the 1990s, NO_2 column densities have been monitored globally from sun-synchronous satellite platforms utilizing the differential optical absorption spectroscopy (DOAS) methodology applied to earth-shine spectra in the visible-blue wavelengths. The nadir spatial resolution of these sensors has generally improved over time—starting with the Global Ozone Monitoring Experiment (GOME) at 40 x 320 km in 1995 (Burrows et al., 1999), dramatically refining a decade later
10   with the Ozone Monitoring Instrument (OMI) at 13 x 24 km in 2004 (Levelt et al., 2006), and improving most recently to a sub-city spatial scale from the TROPOspheric Monitoring Instrument (TROPOMI) instrument aboard Sentinel-5p launched October 2017 with a nadir spatial resolution of 3.5 x 7 km (van Geffen et al., 2019).

     OMI has been a prominent resource for understanding the global distribution of tropospheric NO_2 since its launch. However, short-falls have been documented regarding its inability to capture the spatial variability within polluted regions
15   (e.g., Valin et al., 2011a, Valin et al., 2011b; Broccardo et al., 2018). This inability is further hindered by the use of coarse a priori assumptions in the air mass factor (AMF) calculation for slant-to-vertical column conversion (Heckel et al., 2011; Russell et al., 2011; Goldberg et al., 2017). Though TROPOMI observes NO_2 at a spatial resolution an order of magnitude finer than OMI, its sun-synchronous orbit still limits lower- to mid-latitude observations to the early afternoon hours. However, within the next decade three geostationary air quality monitoring missions will be launched that will be able to
20   monitor daytime air quality hourly at spatial scales of less than 10 km. These missions include observations of North America with Tropospheric Emissions: Monitoring Pollution (TEMPO; Zoogman et al., 2017), Asia with Geostationary Environment Monitoring Spectrometer (GEMS; Kim et al., 2017), and Europe with Sentinel-4/Ultraviolet/Visible/Near-Infrared Instrument (UVN; Ingmann et al., 2012). These geostationary measurements over industrialized regions of the Northern Hemisphere along with ongoing global daily sun-synchronous measurements will be important contributors to the
25   goal of creating an atmospheric composition global observing network (IGACO, 2004; CEOS, 2011).

     To prepare for these planned geostationary air quality missions, NASA supported the development of airborne UltraViolet-VISible (UV-VIS) mapping instruments, (e.g., Geostationary Trace Gas and Aerosol Sensor Optimization: GeoTASO), to help determine the satellite instrument requirements for measurements relevant to air quality and to facilitate retrieval algorithm development at fine spatial resolutions at all times of day (Leitch et al., 2014; Nowlan et al., 2016;
30   Lamsal et al., 2017; Nowlan et al., 2018). These instruments have the capability of retrieving NO_2 at sub-kilometer spatial resolutions which can be useful in assessing trace gas heterogeneity at spatial scales finer than those of current and planned space-based resolutions.

     Measurements from these airborne UV-VIS mapping instruments can provide a transfer standard between the space-based sensor footprints and ground-based spectrometer measurements used for validation of the satellite trace gas
35   products, such as NO_2. The direct-sun DOAS technique used to retrieve NO_2 from ground-based Pandora spectrometer measurements has been shown to be highly precise and accurate due to little uncertainty in the path light travels through the atmosphere (i.e. the air mass factor) at solar zenith angles less than 80 degrees (Herman et al., 2009). Thus, Pandora instruments are a strong candidate for providing a validation standard for trace gas retrievals from geostationary sensors like TEMPO as well as low Earth orbit sensors like TROPOMI. NASA and EPA together have been working toward creating
40   long-term measurement sites across the United States to prepare for and aid satellite product validation and the use of satellite retrievals in air quality management activities (EPA, 2019a). Developments of similar validation site activities are also underway in East Asia and Europe. However, in heterogeneously polluted areas such as cities, the relatively local measurements by Pandora may not necessarily be representative of the spatial scales observed by space-based platforms. High resolution airborne mapping observations provide the unique perspective to assess the impact of spatial scale
45   mismatches between satellite observations and local validation site measurements.

     In 2017, one of NASA's airborne UV-VIS mapping instruments, GeoTASO, was flown aboard the NASA Langley Research Center UC-12b aircraft as part of the Lake Michigan Ozone Study (LMOS; https://www-air.larc.nasa.gov/missions/lmos/index.html) to help characterize NO_2 emission and transport influence on ozone exceedances along the western shore of Lake Michigan. During LMOS, GeoTASO was flown on 21 research fights totalling over 90
50   hours. After LMOS, five research flights were conducted on June 26th and 27th, 2017, totalling 15 hours, in the Los

Angeles (LA) Basin as part of the Student Airborne Research Program (SARP; https://airbornescience.nasa.gov/content/Student_Airborne_Research_Program). In 2017, the LA Basin had the highest 8 h and 1 h ozone concentrations in the United States, as well as the highest annual mean of NO_2 in the United States (EPA, 2019b).

5   This work compares high spatial resolution NO_2 vertical columns retrieved from GeoTASO to those measured from small networks of Pandora spectrometers installed in each region. The high spatial resolution GeoTASO data are then upscaled to spatial resolutions typical of past, present, and planned space-based sensors to demonstrate sensitivity of these comparisons to satellite pixel size in an idealized framework. Finally, these results are compared to two publicly available OMI NO_2 retrievals to provide real-world context. Overall, this work shows the sensitivity of satellite product validation
10   strategies to spatial resolution and begins to demonstrate how the high spatial resolution NO_2 data retrieved from airborne mapping observations can be used with planned high temporal resolution surface observations to evaluate the influence of spatiotemporal heterogeneity on satellite-based trace gas product validation.
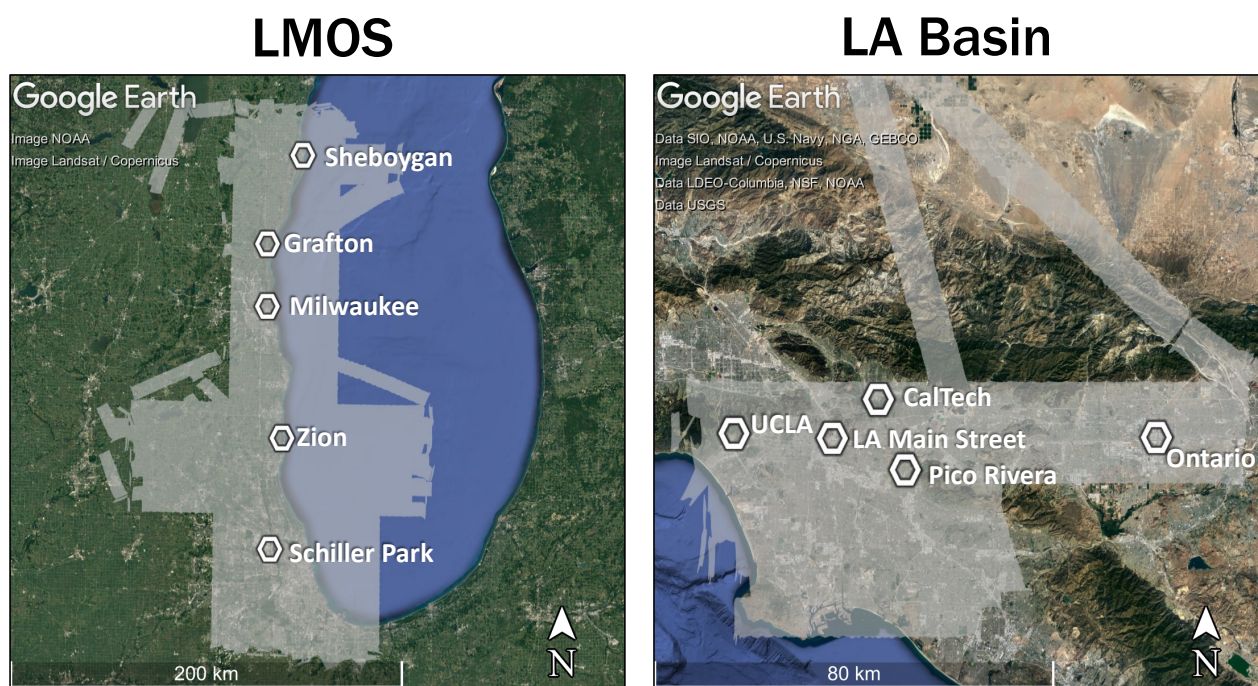
LMOS   LA Basin

Figure 1: Maps of the LMOS and LA Basin regions showing the areas mapped by GeoTASO during summer 2017. The labeled
15   **hexagons indicate locations of Pandora spectrometers operating during the flight days.**

2 Data

2.1 GeoTASO

Geostationary Trace gas and Aerosol Sensor Optimization (GeoTASO) is a hyperspectral mapping instrument built by Ball Aerospace (Leitch et al, 2014) to acquire data for optimizing and testing new high-resolution retrievals of air quality trace
20   gases (NO_2, O_3, and HCHO) and aerosols in preparation for geostationary air quality observations. The instrument is composed of a reflective telecentric telescope that focuses scattered light within its field of view through a photo-elastic modulator for depolarization and lastly into an Offner spectrometer. Within the spectrometer the second order and first order diffracted beams are used to form the ultraviolet (UV) and visible (VIS) spectral ranges, respectively. Each spectral range

(UV, 300 nm to 380 nm, and VIS, 410 nm to 690 nm) is focused onto a separate 2-dimensional charge coupled device (CCD) operated at an integration time of 250 ms for all flights. NO_2 is retrieved using a spectral window within the VIS channel (435-460 nm), which has a spectral resolution (FWHM) of 0.88 nm and a spectral sampling of 3.1 pixels across 1056 pixels (Nowlan et al., 2016).

5 The second dimension of each detector records data in the spatial across-track direction (1033 pixels). GeoTASO observes as a push-broom sensor with an across-track nadir field of view of 45°, providing a swath-width of approximately 7 km from a nominal altitude of 8.5 km. Spectra are coadded to an approximate ground pixel size of 250 x 250 m. During the 2017 GeoTASO flights, gapless maps (otherwise referred to as rasters) were created over an area of interest by executing flight plans composed of parallel flight legs spaced 6 km apart. The overlap in swath between these flight legs provided a
10 tolerance for maintaining gapless coverage during instances of strong cross-winds or when a lower flight altitude was selected in order to operate below high-level thin cirrus clouds. This raster strategy provides data that can easily be spatially co-added to evaluate the influence of spatial resolution on tropospheric NO_2 column measurements, as is shown herein.

Figure 1 shows the areas mapped by GeoTASO during LMOS and in the LA Basin in grey. The entire LMOS domain cannot be mapped during a single flight, therefore individual flight plans focused on sub-portions of the domain
15 where air quality and meteorological forecasts suggested that science goals could be met for each flight. Up to two flights per day were flown during LMOS. In the LA Basin, a single flight plan was developed to maximize coincidences with Pandora spectrometers installed in the region and to extend south to the industrial area near Long Beach, CA. This plan was executed up to three times per day.

NO_2 differential slant columns (DSCs) are retrieved relative to a reference spectrum measured in flight over an area
20 with minimal tropospheric NO_2 absorption features. The retrievals are conducted using QDOAS, an open-source DOAS computing software developed by the Royal Belgian Institute for Space Aeronomy (http://uv-vis.aeronomie.be/software/QDOAS). The resultant DSCs can be physically described as the additional total NO_2 absorption along the path sunlight travels through the atmosphere to the GeoTASO instrument relative to the reference atmosphere. The average fitting uncertainty for the NO_2 DSCs over all flights is 1.2×10^{15} molecules cm^{-2} with a standard deviation of
25 0.25×10^{15} molecules cm^{-2}. Higher solar zenith angles (SZA) and lower albedo result in higher uncertainties. A multi-linear regression indicates that thirty-three percent of the variability in DSC uncertainty is associated with changes in SZA (uncertainty increases with increasing SZA by 0.011×10^{15} molecules cm^{-2} per degree) and almost fifteen percent is associated with variations in surface albedo (uncertainty increases with decreasing albedo by 0.033×10^{15} molecules cm^{-2} per 0.01 decrease in albedo). Additional uncertainty due to using one NO_2 absorption cross section at a single temperature (294 K)
30 leads to a potential bias of $-0.6 \pm 1.7\%$ estimated by the NO_2 profile weighted effective temperature profile in Eq. 4 in Bucsela et al. (2013).

Further processing of DSCs into vertical columns (VCs) requires computations of the AMF: the ratio of the pathlength of light through the atmosphere due to scattering and geometry to the vertical pathlength. AMFs depend on a priori assumptions such as the vertical distribution of NO_2, surface reflectivity, clouds, aerosols, sun angle, and viewing
35 geometry (Palmer et al., 2001; Lamsal et al., 2017). Mathematically, AMFs are the integrated product of (1) scattering weights (the vertical distribution of the instrument sensitivity calculated by a radiative transfer model) and (2) the NO_2 profile shape factor (the relative vertical distribution of NO_2) (Palmer et al., 2001). Scattering weight calculations are most sensitive to inputs that influence light transmission through the atmosphere, most notably from solar and viewing geometry, surface reflectivity, and aerosols (Lamsal et al. 2017; Meier et al., 2017). Scattering weights peak near the altitude of the
40 measurement, decrease with altitude toward the surface, and are higher in areas with bright surface features and higher solar zenith angles (e.g. Fig 4. in Lamsal et al., 2017). This work uses the VLIDORT radiative transfer model to calculate scattering weights (Spurr, 2006). Inputs include atmospheric profiles of temperature, pressure, ozone, NO_2, aerosol, aircraft altitude, viewing geometry, solar geometry, and surface reflectance.

Tropospheric NO_2 profiles are taken from a 12 km hourly analysis of a parallel developmental simulation of the
45 North American Model-Community Multiscale Air Quality (NAM-CMAQ) model from the National Air Quality Forecasting Capability (NAQFC; Stajner et al., 2011). Stratospheric profiles are estimated using the PRATMO chemical box model of stratospheric NO_2 profile climatology (Prather, 1992; McLinden et al. 2000) which estimates NO_2 between approximately 10 and 60 km as a function of month, latitude, and solar zenith angle. This stratospheric model has been used in previous GeoTASO retrievals and has an estimated uncertainty of ~30% in the stratospheric column (Bourassa et al.,
50 2011; Nowlan et al., 2016). Temperature and pressure profiles from the NAM-CMAQ in the troposphere and the Realtime

Air Quality Modeling System (RAQMS; Pierce et al., 2009) up to 60 km are extracted and merged to derive profiles of temperature and pressure, and ozone profiles are extracted from the NAM-CMAQ analysis for the troposphere and OMI gridded monthly climatology in the stratosphere (Liu et al. 2010) for May and June 2017 for input to VLIDORT.

Noguchi et al. (2014) evaluated the influence of surface anisotropy on NO_2 AMFs for geostationary scale
5 measurements using a 1 km MODIS BRDF product and found that, especially in areas with high NO_2 near the surface, not accounting for BRDF in the AMF calculation can lead to large errors. For this reason, this work uses the BRDF RossThick-LiSparse kernels retrieved in Band 3 by the MODIS MCD43A1 daily L3 500m v006 product (Lucht et al., 2000; Schaaf and Wang, 2015). To fill gaps and decrease the noise, this daily product is averaged over a month in the regions GeoTASO measured (May 22nd-June 21nd for LMOS and June 15th-July14th for the LA Basin). Remaining gaps are small and are
10 filled using linear interpolation of nearby pixels. Variations in BRDF derived albedo compare well with the brightness of surface features. Li et al. (2018) found the v006 MCD43A1 product to compare very well with Multi-angle Imaging SpectroRadiometer (MISR) land surface reflectance with little bias and a high correlation (r=0.95 in a case study for northeast Asia region).

Clouds and aerosols are not considered in the AMF calculation in this work. Cloud affected pixels are excluded
15 from analysis by removing pixels having detector count rates of greater than $2.5x10^4$ counts s^{-1} within the DOAS NO_2 spectral window. Aerosols can cause decreases or increases in AMF depending on their radiative properties, loading, and altitude relative to the location of NO_2 (Leitao et al., 2010; Tack et al., 2019). Lamsal et al. (2017) show that sensitivity of tropospheric AMF to aerosol loading is less than 20% for AOD values between zero and 1.0. During these 2017 flights, aerosol loadings were generally light. In both study domains, one Cimel sunphotometer was operating during flight days
20 (https://aeronet.gsfc.nasa.gov/cgi-bin/bamgomas_interactive). At the Zion site during LMOS, AOD was generally below 0.1 on flight days with a peak reported of ~0.2 after cloud filtering. In the LA Basin, there were no data reported for the June 26th, 2017 flight day, but AODs were less than 0.1 on June 27th, 2017. Given the relatively low aerosol loadings, errors in AMF due to neglecting aerosols are expected to be small for these flights (< 5% using sensitivities shown by Lamsal et al. (2017)).
25 Differential slant columns are converted into below aircraft vertical columns using the following the equation (simplified from Sect 3.3 in Lamsal et al., 2017):

$$VC_{below} \text{ or } TropVCs = \frac{DSC - VC_{above}AMF_{above} + reference\ column}{AMF_{below}}, \qquad (1)$$

Where DSC is the differential slant column, $VC_{above/below}$ is the vertical column above and below the aircraft, and $AMF_{above/below}$ is the calculated AMF above and below the aircraft. From the merged NAM-CMAQ/PRATMO columns, the
30 reference total vertical column is assumed as $5.5x10^{15}$ molecules cm^{-2} for LMOS and $3.8x10^{15}$ molecules cm^{-2} for SARP (~60% and 75% stratospheric for LMOS and SARP, respectively). As NO_2 column variations in the troposphere are largely confined to the boundary layer, this work assumes that residual tropospheric variations in the above-aircraft column are negligible and the below aircraft vertical columns are referred to as tropospheric vertical columns (TropVCs). Figure 2 shows examples of NO_2 TropVCs (top) and tropospheric AMFs (middle) for a morning flight over Chicago, IL on June 1st,
35 2017 (left) and a morning flight over the LA Basin from June 26th, 2017 (right). The bottom row of Fig. 2 shows base maps from Google Earth Pro to aid identification of surface features in the maps above. In the areas mapped in Fig. 2, NO_2 TropVC spans roughly two orders of magnitude and spatial patterns are consistent with emission sources, such as busy roadways, airports, and industrial regions.

20170601 Morning Chicago Raster   **20170626 Morning LA Basin Raster**
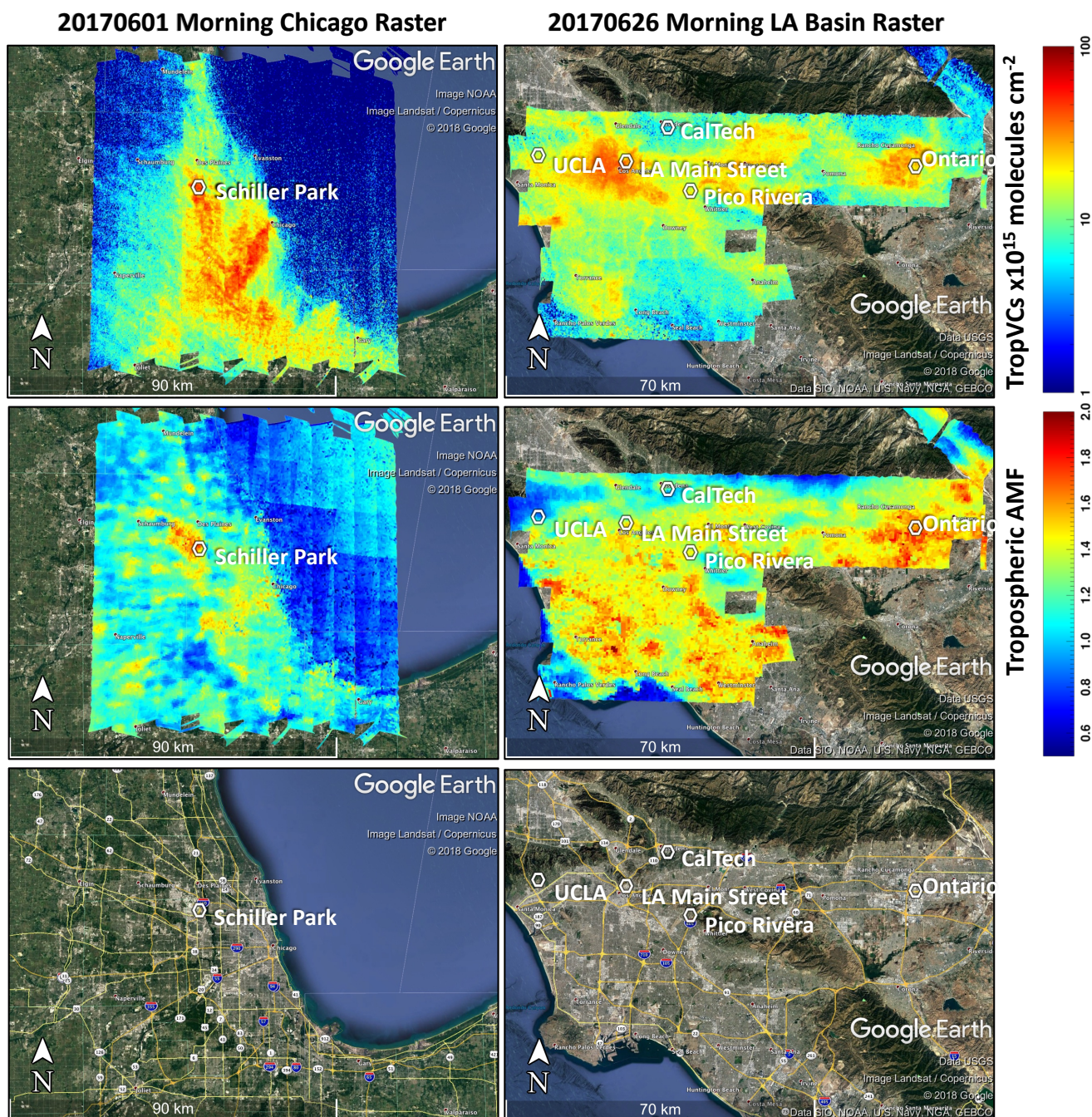
Figure 2: Tropospheric NO₂ vertical column on a log10 color scale (top), tropospheric AMF on a linear color scale (middle), and base map (bottom) for a Chicago raster on the morning of June 1st, 2017 (left) and an LA Basin raster on the morning of June 26th, 2017 (right). The base maps show roadways, urbanized areas, and surface characteristics. The labeled hexagons indicate locations of Pandora spectrometers.

Over land, large spatial variations of tropospheric AMF are evident, associated primarily with the surface reflectance characteristics. A multi-variable linear regression of these data indicates that surface albedo explains 64% of the variability in tropospheric AMF, illustrating the importance of accurately treating surface reflectance in these high spatial resolution retrievals. Over an area with homogeneous surface reflectance (over Lake Michigan east of Chicago), the subtle
5 influence of a varying NO_2 shape factor is visible in the AMF, but has little impact on the magnitude of TropVC because there is little NO_2 in this location. A priori NO_2 profile accounts for 16% of the variability in tropospheric AMF. Viewing geometry has smaller effects, with SZA accounting for 1.8% of the variability and the relative azimuth angle and viewing zenith angle causing even smaller amounts.

To better gauge the sensitivity of AMF and TropVC to the NO_2 vertical profile in the troposphere, the AMFs
10 calculated for the most polluted LMOS flight (June 1st, 2017; Fig. 2) were compared to AMFs calculated using a single median NAM-CMAQ NO_2 vertical profile (not shown). This median profile is representative of a moderately polluted urban area with a tropospheric NO_2 column of 3.6×10^{15} molecules cm^{-2}, most of the NO_2 in the lowest km of the atmosphere, and an NO_2 maximum at the surface of approximately 4 ppbv. The resulting differences in AMF can be large, ranging from -30% to 10%, however the largest AMF differences occur over relatively clean areas in which the median polluted profile is less
15 representative. The differences in TropVCs are about $\pm 1 \times 10^{15}$ molecules cm^{-2} at the 5th/95th percentiles with 50% of the points having differences between -0.2×10^{15} and 0.5×10^{15} molecules cm^{-2}. These values are on the same order of magnitude as the uncertainty in DSCs.

To estimate total uncertainty in the TropVC, error propagation was applied to Eq. (1). Assuming a 50% uncertainty in the NAM-CMAQ profile, 30% in the PRATMO profiles, and a conservative 30% uncertainty in the below aircraft AMF
20 (largest percent variation in the sensitivity study discussed in the previous paragraph), the uncertainty in the reference is estimated to be 2.3×10^{15} molecules cm^{-2} for LMOS and 1.9×10^{15} molecules cm^{-2} for SARP. The average uncertainty in the above aircraft vertical column is 1.3×10^{15} molecules cm^{-2} with a standard deviation of 0.08×10^{15} molecules cm^{-2}. The median total uncertainty for TropVCs for both regions combined is 2.3×10^{15} molecules cm^{-2}. Percent uncertainty (5th-95th percentile) ranges from 46-143% for relatively unpolluted columns ($< 5 \times 10^{15}$ molecules cm^{-2}), from 32-60% for moderately
25 polluted columns ($5-15 \times 10^{15}$ molecules cm^{-2}), and ~30% for polluted columns ($> 15 \times 10^{15}$ molecules cm^{-2}). These values are similar to those calculated by Nowlan et al. (2016).

2.2 Pandora

Pandora is a UV/VIS ground-based spectrometer used to retrieve trace gas column amounts (Herman et al., 2009; Herman et al., 2015). While the instrument has the capability to make both direct-sun and all-sky radiance measurements from which
30 trace gas amounts can be retrieved, only the direct-sun retrievals are used in this work due to their high precision and accuracy. The direct-solar beam is measured by Pandora via an optical head sensor attached to a solar tracker. The solar beam is carried to the UV/VIS spectrometer by a fiber optic cable attached to the head sensor. NO_2 is retrieved by applying a spectral fitting algorithm (Cede, 2017) using a near-noon reference spectrum, from which the NO_2 slant column amount is derived by a statistical calibration approach (Herman et al., 2009). A geometric AMF is used for the slant-to-vertical column
35 conversion as the path length through the atmosphere is dominated by the direct solar beam rather than scattered light through the atmosphere (Cede, 2017). Precision and accuracy of the instrument are reported as 2.67×10^{14} and 2.67×10^{15} divided by AMF molecules cm^{-2}, respectively, by Herman et al. (2009).

The LMOS region and the LA Basin each had 5 Pandoras operating within the research area during GeoTASO flight days (hexagons in Fig. 1). Their names and coordinates are listed in Table 1. In this work the Pandora retrievals are
40 screened to exclude observations with vertical column error greater than 0.05 DU and normalized RMS greater than 0.005, to limit the retrieval uncertainty to approximately 10%.

Table 1: Pandora site names and locations in the LMOS and LA Basin domains. These locations are also indicated by hexagons on the maps in Figure 1.

Pandora Site	Location
LA Main Street	34.066°N, -118.227°W
Ontario	34.068°N, -117.526°W
UCLA	34.074°N, -118.441°W
Pico Rivera	34.010°N, -118.069°W
CalTech	34.136°N, -118.127°W
Sheboygan	43.746°N, -87.709°W
Grafton	43.343°N, -87.920°W
Zion	42.468°N, -87.810°W
Schiller Park	41.965°N, -87.876°W
Milwaukee	43.061°N, -87.914°W

2.3 Ozone Monitoring Instrument (OMI)

5 OMI is a space-based UV/VIS instrument launched in 2004 aboard the EOS-Aura satellite in a sun synchronous orbit with an equator crossing time in the early afternoon (Levelt et al., 2006). This work uses the NASA Standard Product (SP) Version 3 (Krotkov et al., 2017) and the Berkeley High Resolution (BEHR) Product (Russell et al., 2011; Laughner et al., 2018; Laughner et al., 2019) to assess how the column retrievals compare with measurements from Pandora spectrometers deployed during summer 2017 in the domains of LMOS and the LA Basin. The two vertical column products are based on
10 the same slant columns (produced by the NASA Standard Product retrieval) but they differ in their a priori inputs for the air mass factor calculation (i.e. albedo, terrain pressure, and NO_2 profiles; http://behr.cchem.berkeley.edu/TheBEHRProduct.aspx). As the name suggests, the BEHR a priori have a higher spatial resolution than the NASA Standard Product (Russell et al., 2011; Laughner et al., 2019). OMI data used here are filtered to exclude cloud fractions (derived from MODIS) greater than 20% (following criteria defined in Laughner et al. (2019)) and
15 data from OMI's row anomaly (http://projects.knmi.nl/omi/research/product/rowanomaly-background.php). From 2004 until October 2017, OMI had the finest spatial resolution of any NO_2 retrieving sensor in low Earth orbit. Before the appearance of the row anomaly in 2007, the finest pixel size of OMI was approximately 13 x 24 km at nadir. In January 2009, the row anomaly extended to affect nadir pixels and during summer 2017 the pixel areas coincident with the campaign Pandora observations ranged from 365 km^2 near-nadir to approximately 4600 km^2 at the edge of the swath.

20 **3 Results**

3.1 Comparison of airborne GeoTASO and ground-based Pandora retrievals

Pandora spectrometer measurements have been previously used to validate retrieval products from GeoTASO and similar airborne mapping spectrometers during intensive campaigns (Nowlan et al., 2016; Lamsal et al., 2017; Nowlan et al., 2018). Figure 3 shows the comparison between the 80 coincident Pandora and GeoTASO TropVC observations during LMOS and
25 the LA Basin flights colored by ground site. The first five ground sites in the legend correspond to Pandoras installed in the LA Basin and the last five are located in the LMOS domain. Coincidences are identified as the median of all cloud-free GeoTASO TropVCs having pixel centers within a 750 m radius of a Pandora for each overpass (minimum requirement of 16 valid GeoTASO 250 x 250 m pixels for a spatial coverage of at least 1 km^2) and the Pandora column observed closest in time to the GeoTASO overpass (within ± 5 minutes). A Pandora TropVC is derived by subtracting the stratospheric vertical
30 column calculated with the PRATMO model from the Pandora total column, following the same approach used with

GeoTASO data. Coincidences without at least two valid Pandora data points within ± 5 minutes of the GeoTASO overpass are excluded because acquisition of only a single Pandora data point within ten minutes indicates likely periodic clouds or poor solar tracking by the instrument. TropVCs from GeoTASO compare well with Pandora, with high correlation (r^2=0.91), a slope of 1.03, and an offset of 0.52×10^{15} molecules cm^{-2}.

5   The whiskers in Fig. 3 indicate the 10th and 90th percentiles of GeoTASO TropVCs within the 750 m radius for GeoTASO (vertical whiskers) and the maximum and minimum Pandora TropVC within ± 5 minutes from the GeoTASO overpass (horizontal whiskers, representing 6-7 valid Pandora measurements for most of these coincidences), providing a glimpse of the spatiotemporal variability at the time of the coincidence. Generally, spatial variability (vertical whiskers) increases as the magnitude of NO$_2$ increases. An exception to this pattern occurs at the Zion site. Zion has the lowest surface
10   albedo of any site, ranging from 1.3-2.6% depending on SZA. The lower albedo over the Zion region together with the relatively low NO$_2$ amounts lead to a lower signal-to-noise ratio in the GeoTASO observations, resulting in a higher uncertainty in the DOAS spectral fit (as discussed in Sect. 2.1). Therefore, the large vertical whiskers at this site are indicative of increased uncertainty in the retrieval in addition to spatial heterogeneity.
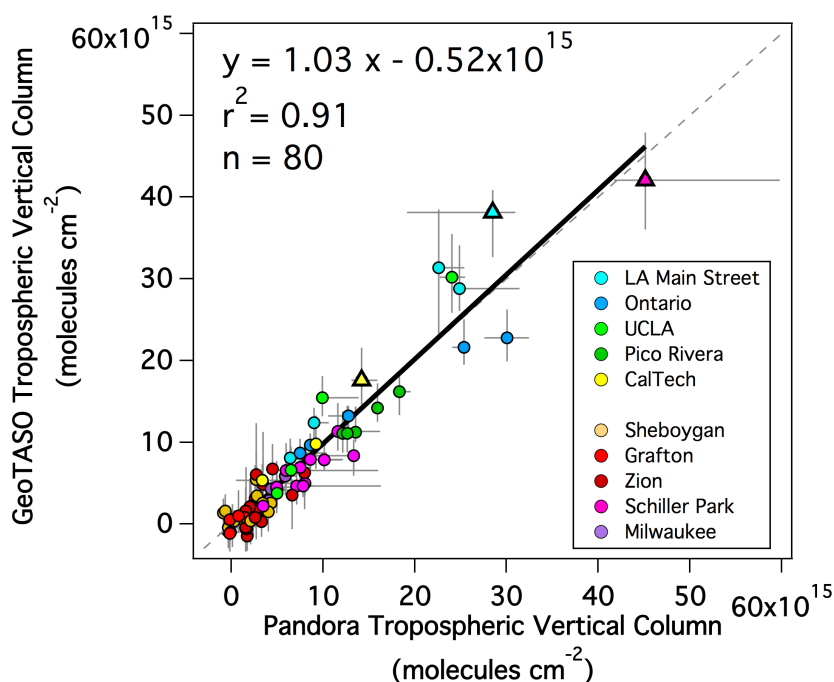
15   **Figure 3: Scatter plot of GeoTASO NO$_2$ TropVCs vs. Pandora NO$_2$ TropVCs colored by Pandora site. Vertical whiskers show the 90th and 10th percentiles of GeoTASO TropVCs within the 750 m radius of the Pandora site. Horizontal whiskers show the maximum and minimum Pandora TropVCs within the ± 5-minute coincidence window. Triangles indicate coincidences discussed within Sect. 3.1. The grey dashed line indicates the 1:1 line.**

20   The largest temporal variability (horizontal whiskers) occurs at the Schiller Park site in Chicago, IL, which is located along a major highway near the end of a Chicago O'Hare airport runway. High temporal variability is common at the site and is likely due to local emissions associated with air traffic and nearby roadways. The most polluted point of all coincidences occurs at Schiller Park on June 1st, 2017 (pink triangle in Fig. 3) and this case is further explored in Fig. 4(a). Figure 4(a) shows a map of the GeoTASO NO$_2$ TropVCs and a hexagon depicting the Pandora location which is colored by
25   the NO$_2$ column observed by Pandora nearest in time to the GeoTASO overpass. The 750 m radius used to define coincident GeoTASO data and an arrow depicting the direction in which Pandora is observing are overlaid. GeoTASO observed a median of 42×10^{15} molecules cm^{-2}, whereas the Pandora observed 45×10^{15} molecules cm^{-2}. Inside the 750 m radius, NO$_2$ columns range between 30 and 50×10^{15} molecules cm^{-2}, and the highest columns observed occur along the viewing direction of Pandora. Figure 4(b) shows a time series of the Pandora TropVC surrounding this overpass and the GeoTASO

coincidence. Within an hour prior to the overpass, large temporal variations in NO_2 column are observed by the Pandora, suggestive of small-scale plumes influencing the site. In the 10-minute Pandora window (grey section), Pandora peaks at over 60×10^{15} molecules cm^{-2}. If any temporal averaging is applied to Pandora data in this case, the coincidence would yield a larger apparent difference between GeoTASO and Pandora. The tremendous amount of variability at this highly
5 heterogeneous location suggests caution for use in applications such as satellite validation.

While the 80 GeoTASO/Pandora coincidences are highly correlated with a slope near 1:1, there are a few outliers that deviate from the linear regression line by amounts larger than the range of observed variability by either instrument. Some of these outliers can be attributed to mismatches in spatial representativeness, as the viewing geometry of the Pandora spectrometer is always oriented in the direction of the sun while the GeoTASO median is constructed from pixels within the
10 750 m radius centered on the Pandora location extending into all directions. Figure 5 highlights one of these cases (yellow triangle in Fig. 3). On June 27th, 2017, over the CalTech site in the LA Basin, Pandora observes a column during the overpass of approximately 14×10^{15} molecules cm^{-2} whereas the GeoTASO spatial median is 18×10^{15} molecules cm^{-2}. The GeoTASO TropVC map (Fig. 5 (a)) shows that Pandora is observing in a direction where NO_2 values are at a local minimum, such that the GeoTASO median within the 750 m radius is about 30% higher than Pandora while the GeoTASO
15 TropVCs along the viewing direction of Pandora at that time are more similar to the Pandora observations. Pandora TropVCs are varying slowly in time surrounding the GeoTASO overpass (Fig. 5(b)). Together these characteristics suggest that the differences between these two observations are more likely associated with the spatial criteria assumed for this comparison rather than temporal variability at the time near the coincidence. Some of the other coincidences showing notable differences, including the two most polluted Ontario points (both lying below the 1:1 line with concentrations of 20-
20 25×10^{15} molecules cm^{-2}) also appear to be associated with the assumption in spatial criteria (not shown). Future comparisons of Pandora to high-spatial resolution airborne data could consider the Pandora viewing geometry in the coincidence criteria, but this is not a viable option for validating satellite products which are not as spatially refined.
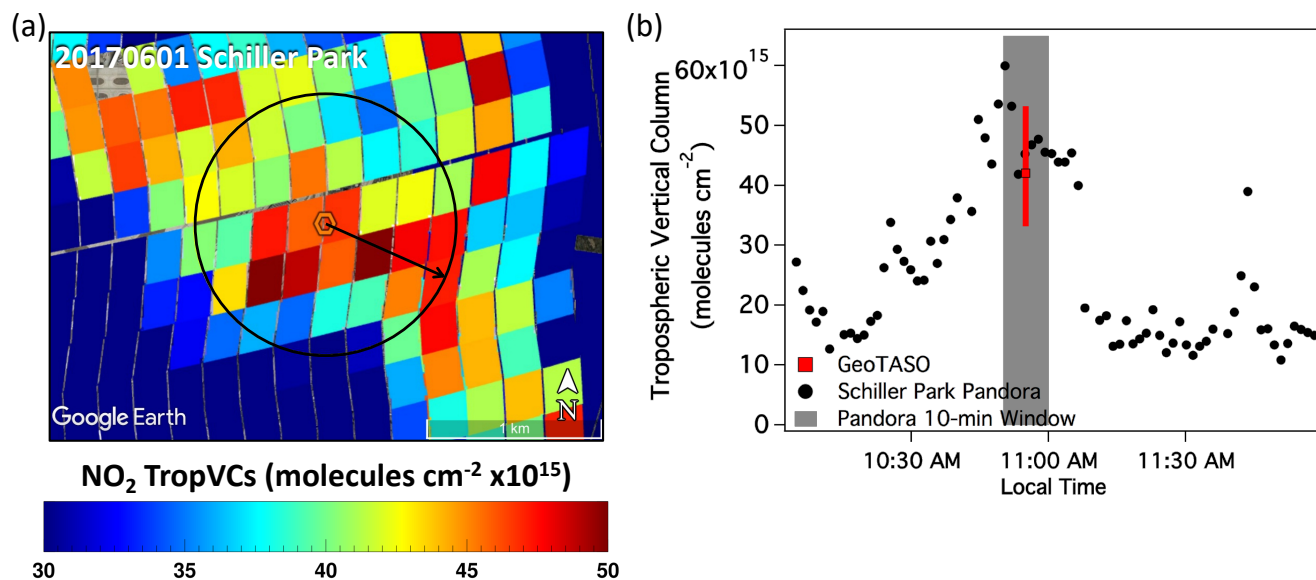
Figure 4: (a) Map of GeoTASO TropVCs on a linear color scale for the Schiller Park overflight on June 1st, 2017 at 15:55 UTC
25 **(10:55 LDT) (pink triangle in Figure 3) with the 750 m radius considered in the spatial binning of GeoTASO overlaid and an arrow depicting the Pandora viewing direction (solar azimuth angle) during the overpass time. The Pandora hexagon is colored by the NO_2 TropVC measured by Pandora during the overpass. (b) Time series showing Pandora data (black points) within approximately ± 1 hour of the GeoTASO overpass. The Pandora temporal window for the coincidence is shaded in grey and the GeoTASO TropVC and 10th-90th percentiles from the overpass are shown in red.**
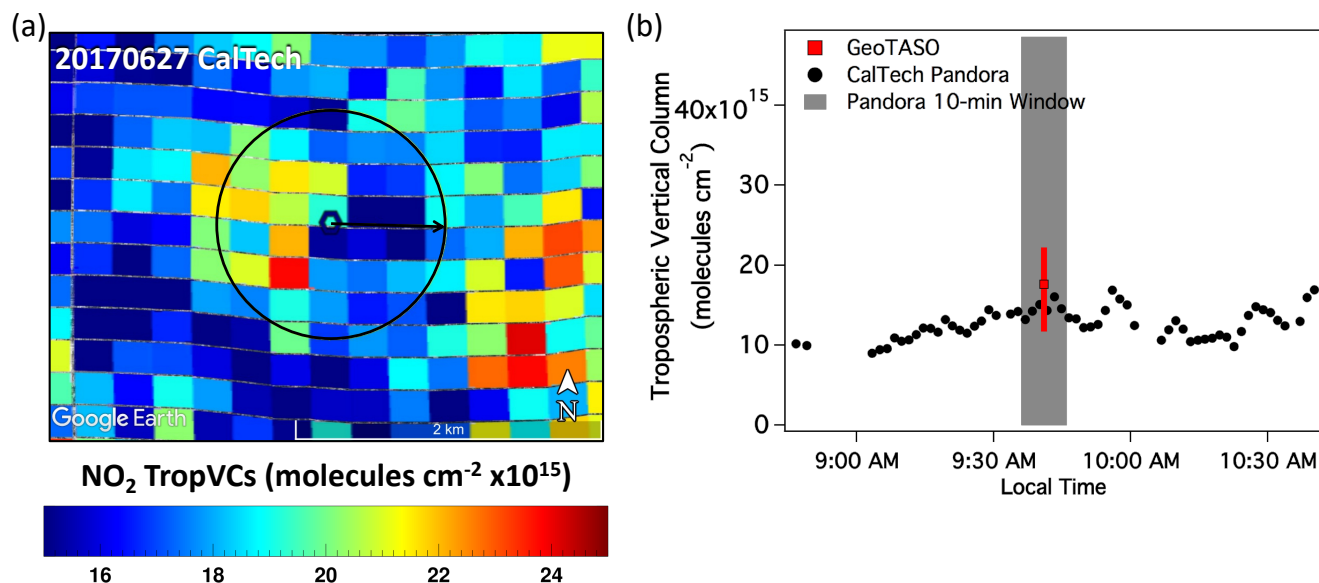
Figure 5: (a) Map of GeoTASO TropVCs on a linear color scale for the CalTech overflight on June 27th, 2017 at 16:41 UTC (09:41 LDT) (yellow triangle in Figure 3) with the 750 m radius considered in the spatial binning of GeoTASO overlaid and an arrow depicting the Pandora viewing direction (solar azimuth angle) during the overpass time. The Pandora hexagon is colored by the

5 **NO$_2$ TropVC measured by Pandora during the overpass. (b) Time series showing Pandora data (black points) within approximately ± 1 hour of the GeoTASO overpass. The Pandora temporal window for the coincidence is shaded in grey and the GeoTASO TropVC and 10th-90th percentiles from the overpass are shown in red.**
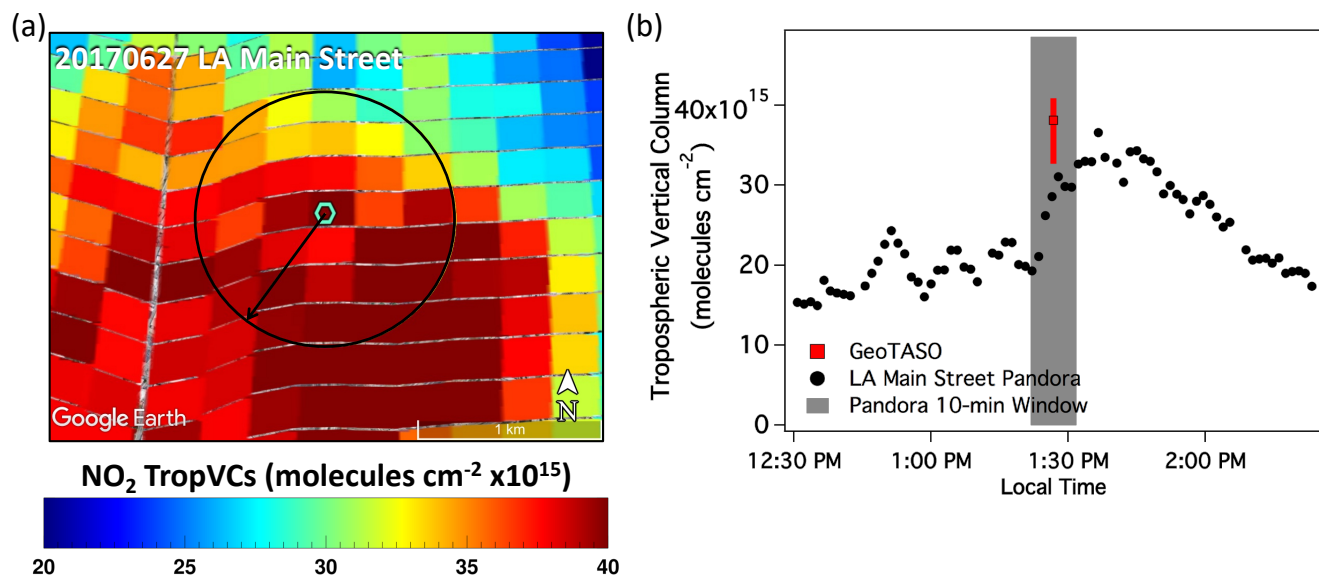
Figure 6: (a) Map of GeoTASO TropVCs on a linear color scale for the LA Main Street overflight on June 27th, 2017 at 20:26 UTC

10 **(13:26 LDT) (cyan triangle in Figure 3) with the 750 m radius considered in the spatial binning of GeoTASO overlaid and an arrow depicting the Pandora viewing direction (solar azimuth angle). The Pandora hexagon is colored by the NO$_2$ TropVC measured by Pandora during the overpass. (b) Time series showing Pandora data (black points) within approximately ± 1 hour of the GeoTASO overpass. The Pandora temporal window for the coincidence is shaded in grey and the GeoTASO TropVC and 10th-90th percentiles from the overpass are shown in red.**

The largest outlier from the regression line of Pandora-to-GeoTASO coincidences occurs at LA Main Street on the afternoon of June 27th, 2017 (blue triangle in Fig. 3), where GeoTASO observes a TropVC of 38×10^{15} molecules cm^{-2} and the Pandora TropVC is only 28×10^{15} molecules cm^{-2}. This coincidence also shows large gradients both spatially and temporally. What is unique about this case is the environmental/meteorological conditions present during this time period

5 that make data comparisons and GeoTASO retrieval challenging. Figure 6 has the same formatting as Fig. 4 and Fig. 5. Focusing on the ten-minute window used in the temporal matching of Pandora data, Pandora NO_2 TropVC increases from 20×10^{15} molecules cm^{-2} to over 30×10^{15} molecules cm^{-2}. This feature is caused by the arrival of a sea breeze front passing through from the southwest at this time which acts as a convergence zone accumulating NO_2 along this front as it passes through the LA Basin (Judd et al., 2018). In this case, because the Pandora data show a rapid increase, any temporal

10 averaging window placed on the Pandora data for data comparison would not be representative of the conditions during the overpass (similar to the coincidence shown in Fig. 4). Pandora reaches a peak within this 10-minute window of 31×10^{15} molecules cm^{-2} approximately one minute after GeoTASO overpasses, which is closer to the magnitude observed by GeoTASO but still about 7×10^{15} molecules cm^{-2} lower. Within 5-10 minutes after the overpass, Pandora values rise again to a range of 33-37×10^{15}, almost as large as GeoTASO median value. Figure 6(a) indicates that directionality does not reconcile

15 the observations as GeoTASO NO_2 TropVCs in the direction Pandora is viewing are consistently larger than Pandora observations, suggesting a potential high bias in the GeoTASO TropVC in this case. High bias could be caused by an underestimation of the AMF; the tropospheric AMF would have to increase from 1.3 to ~1.75 for this area to yield a TropVC similar to Pandora. Given the unique circumstances of the sea breeze front, and the relatively coarse resolution of the NAM-CMAQ model used to obtain the NO_2 profile (12 km), we speculate that perhaps the shape factor used in the AMF

20 calculation may not be representative of the actual NO_2 vertical profile within the sea breeze circulation during this time. The rapid fluctuations in Pandora observations through this period also suggest that the airmass is not well mixed, i.e., eddies likely exist in the vicinity of this front which could affect vertical structure at very localized scales. Another contribution could be inaccuracies in the AMF associated with surface reflectance at this site. All LA Main Street coincidences lie above the 1:1 line in Fig. 3 (GeoTASO TropVC is consistently larger than Pandora), which could be caused by a low bias in the

25 BRDF weighting kernels. LA Main Street is in an area that has fewer valid retrievals from the MCD43A1 product during the monthly average used for BRDF input to VLIDORT. Further investigation of systematic biases by site due to BRDF uncertainty would require more consistent sampling at the site, which will be possible with satellite products and long-term Pandora measurements used for product validation in the future.

Table 2: Statistics between Pandora and the GeoTASO data at the nominal pixel size shown in Figure 3 as well as the
30 **simulated pixel sizes for TEMPO, TROPOMI, and OMI products shown in Figure 9.**

Pixel Size	All Points				Pandora < 40×10^{15} molecules cm^{-2}				Pandora < 20×10^{15} molecules cm^{-2}			
	slope	Intercept x10^{15}	r^2	N	slope	Intercept x10^{15}	r^2	N	slope	Intercept x10^{15}	r^2	N
Nominal:	1.03	0.52	0.91	80	1.08	-0.75	0.89	79	0.96	-0.30	0.84	73
TEMPO: 3 x 3 km	0.88	-0.07	0.86	79	1.03	-0.72	0.89	78	0.93	-0.35	0.85	72
TROPOMI: 5 x 5 km	0.77	0.11	0.88	76	0.88	-0.32	0.89	75	0.87	-0.36	0.81	69
OMI: 18 x 18 km	0.57	0.9	0.61	66	0.73	0.01	0.83	65	0.89	-0.7	0.78	60
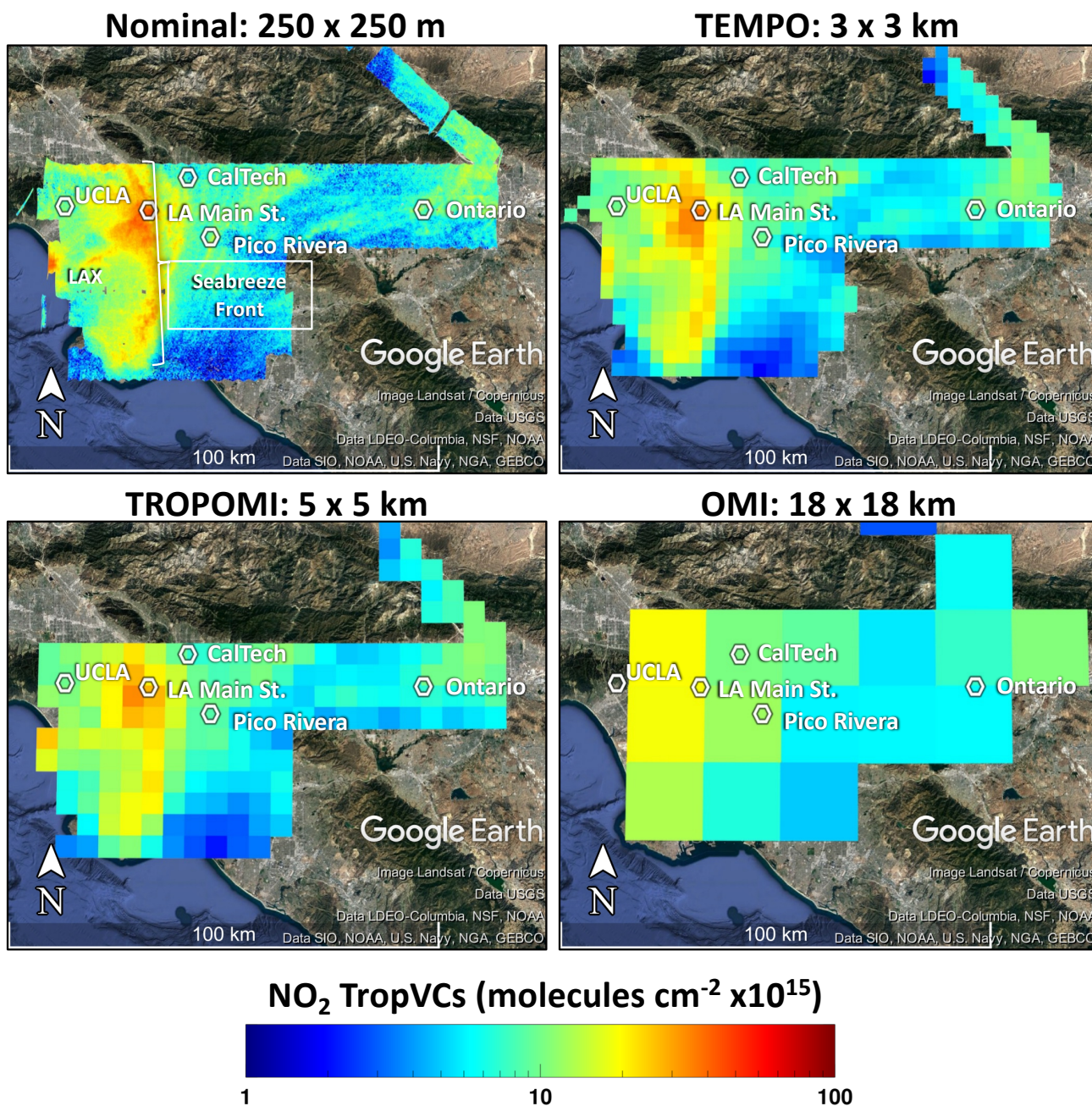
Figure 7: Maps of GeoTASO NO₂ TropVC on a log10 color scale averaged to the labeled pixel sizes to demonstrate the spatial detail that would be observed from the midday raster in Los Angeles on June 27th, 2017. All pixels shown have at least 30% of their area mapped by GeoTASO during this timeframe.
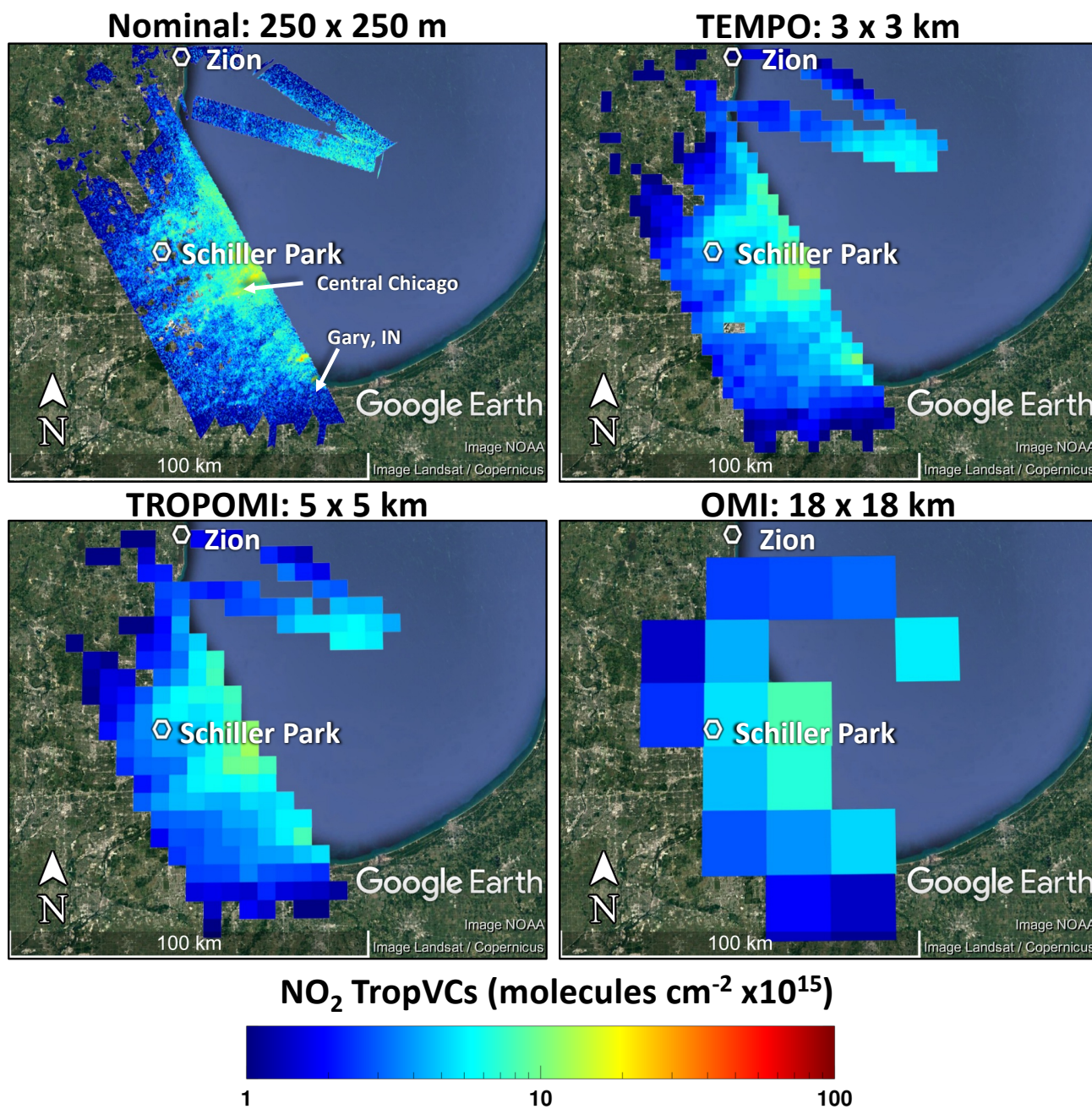
Figure 8: Maps of GeoTASO NO$_2$ TropVC on a log10 color scale averaged to the labeled pixel sizes to demonstrate the spatial detail that would be observed from the midday in the Chicago area on May 22nd, 2017. All pixels shown have at least 30% of their area mapped by GeoTASO during this timeframe.

3.2 Scaling GeoTASO to satellite product footprints

Past, present, and planned satellite instruments have spatial resolutions that are coarser than the GeoTASO airborne measurements. The gapless mapping strategy executed with GeoTASO during summer 2017 provides fine-resolution data suitable for averaging to coarser areal resolutions typical of these current and next-generation satellite retrievals. As

5 demonstrated by the good agreement between Pandora and GeoTASO shown in Sect 3.1, the GeoTASO observations during these rasters capture the spatiotemporal variability existing in these areas. Comparisons of upscaled GeoTASO retrievals with Pandora measurements provide an early assessment of the capabilities of the next-generation sensors for resolving urban scale NO_2 and also give insight to validation strategies in urban regions, where sub-pixel variability within the satellite product footprint may be significant.

10   To simulate the satellite products, each GeoTASO raster is averaged to fixed grids with pixel areas representative of near-nadir observations from TEMPO, TROPOMI, and OMI. These grids are simplified by making each pixel square in shape to avoid introducing an orientation bias. Simulated pixels are 3 x 3 km ($9 km^2$) for TEMPO (literature reported 9.24 km^2 per pixel, Zoogman et al., 2017), 5 x 5 km ($25 km^2$) for TROPOMI (literature reported $24.5 km^2$, van Geffen et al., 2019), and 18 x 18 km ($324 km^2$) for OMI (FoV75Area for nadir is $338.4 km^2$).

15   GeoTASO data are remapped to these fixed grids by computing a weighted average of the GeoTASO TropVCs based on the areal overlap within each simulated satellite grid pixel for each raster. Figure 7 shows an example of this process for the midday Los Angeles raster on June 27th, 2017, at the nominal GeoTASO resolution and each simulated satellite product resolution. At this time, a marine/land airmass convergence zone was created by the development of a sea breeze which resulted in an accumulation of NO_2 seen as a line of enhanced NO_2 in excess of 30×10^{15} molecules cm^{-2}

20 extending north and south of LA Main Street (discussion of Fig. 6, Sec. 3.1; Judd et al., 2018). A plume is also seen extending inland from the Los Angeles International Airport (LAX). As expected, fine scale features evident in the native GeoTASO observations are increasingly blurred as the spatial resolution is degraded. The airport plume is spatially distinct up to the TEMPO spatial scale and the sea breeze is resolved through the TROPOMI spatial scale, but neither are visible at the spatial scale of OMI.

25   Another example is shown in Fig. 8 for a Chicago raster near midday on May 22nd, 2017. In this example, the southwesterly wind throughout the day quickly advected local emissions out over Lake Michigan, allowing visualization of fresh emission source regions and broadening and accumulation of the resulting pollution plume as it passes over the Chicago metropolitan area. The native-resolution GeoTASO retrievals show three areas of enhanced NO_2: near Schiller Park-O'Hare Airport, central Chicago, and the industrial shore near South Chicago and Gary, IN. This raster was repeated 3

30 other times on this day, and all four rasters show a similar spatial pattern but differing magnitudes of NO_2 TropVCs (not shown). These spatial features are discernible up through the areal resolution of TROPOMI but not at the OMI scale. The maximum observed at an OMI resolution is even displaced, such that it does not accurately represent the location of the highest NO_2 TropVCs.

     To quantify the relationship between the simulated satellite pixels and Pandora data, the coincidence-based analysis

35 of Sect. 3.1 is repeated for each equivalent upscaled resolution. Fig. 9 shows the scatter plots of these coincidences and the associated linear regression statistics are shown in Table 2. To avoid excess extrapolation, only upscaled grid cells that are at least 30% sampled by GeoTASO are considered in this analysis, which is why the number of coincidences decreases as pixel size increases (Table 2).

     As the pixel size increases, the inability to resolve smaller scale polluted plumes results in larger deviation from the

40 1:1 agreement with slope decreasing from 0.88 at a TEMPO scale to 0.77 and 0.57 at TROPOMI and OMI scales, respectively. The decrease in slope is partially driven by the most polluted coincidence at Schiller Park. Figure 10 shows this coincidence (zoomed out map from Fig. 4) with the upscaled equivalent pixels from TEMPO, TROPOMI, and OMI overlaid. The plume observed by GeoTASO and Pandora in this case is smaller than the spatial scale of a TEMPO pixel with a simulated-satellite value that decreases quickly from 42×10^{15} molecules cm^{-2} at native GeoTASO resolution to

45 30×10^{15} molecules cm^{-2} at simulated TEMPO resolution (Pandora is located inside the left TEMPO pixel in the map though the two nearest TEMPO pixels are shown in Fig. 10 to contemplate placement of Pandora in the TEMPO grid as its placement is near the pixel edge and does not appear to be a factor). This illustrates the challenge of determining the difference between retrieval bias and mismatched spatial representation. In this analysis, the native resolution retrieval does not appear to be biased (Sect. 3.1). Therefore, the changes in the relationship between upscaled GeoTASO observations and

Pandora are solely due to spatial representation. In the case of this coincidence with its high degree of spatial and temporal variability, none of the simulated satellite products are capable of resolving the plume observed by GeoTASO and Pandora, and without careful analysis the satellite products would appear to have a low bias.
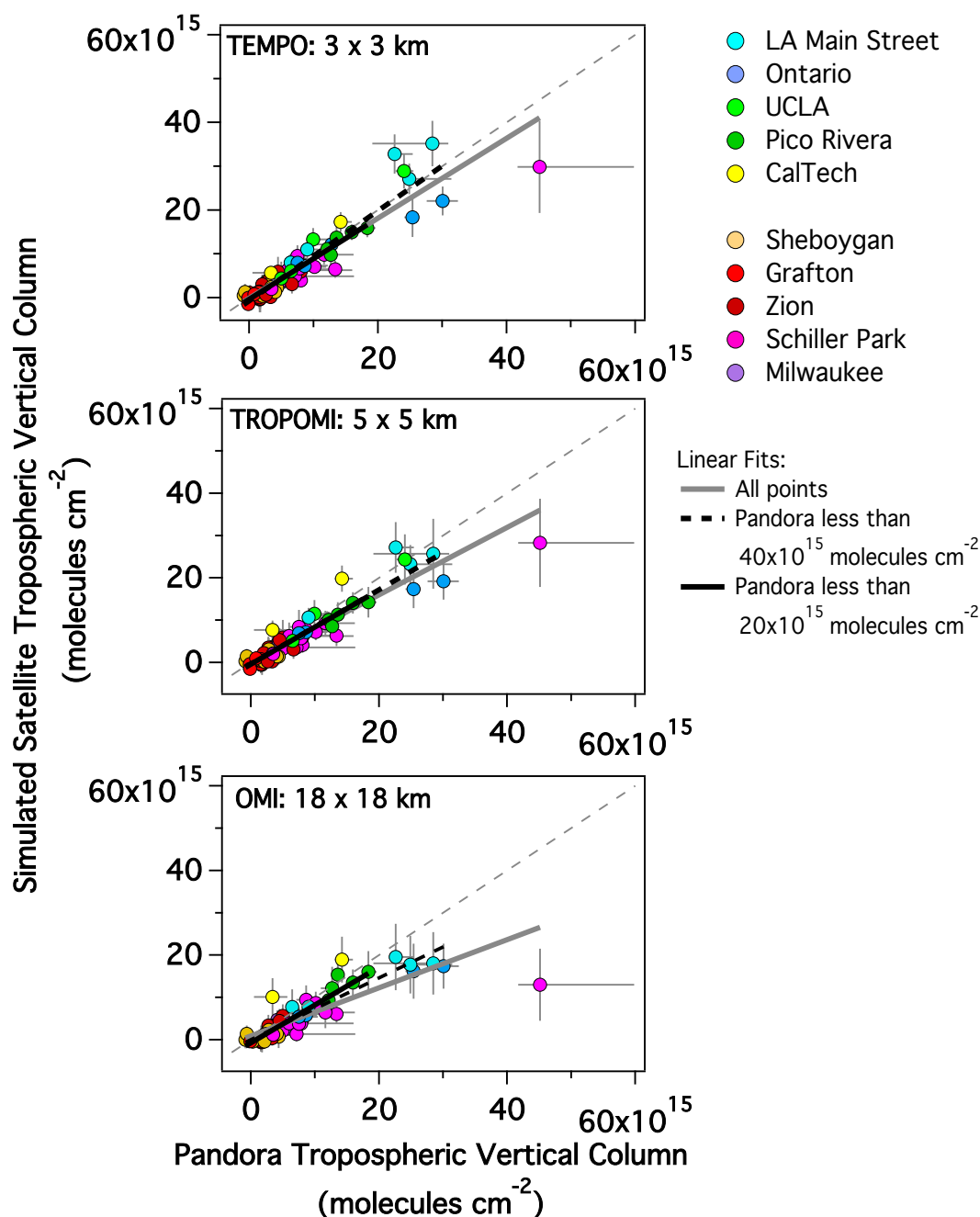
Figure 9: Scatter plot of GeoTASO TropVCs scaled to the nadir areal resolution of TEMPO (a), TROPOMI (b), and OMI (c) TropVCs vs. Pandora TropVCs colored by site and their associated linear fits. Vertical bars show standard deviation of GeoTASO TropVCs within the upscaled pixel. Horizontal bars show the minimum and maximum of Pandora data within the ± 5-minute coincidence window. The grey dashed line indicates the 1:1 line.

NO₂ TropVCs x10¹⁵ molecules cm⁻²
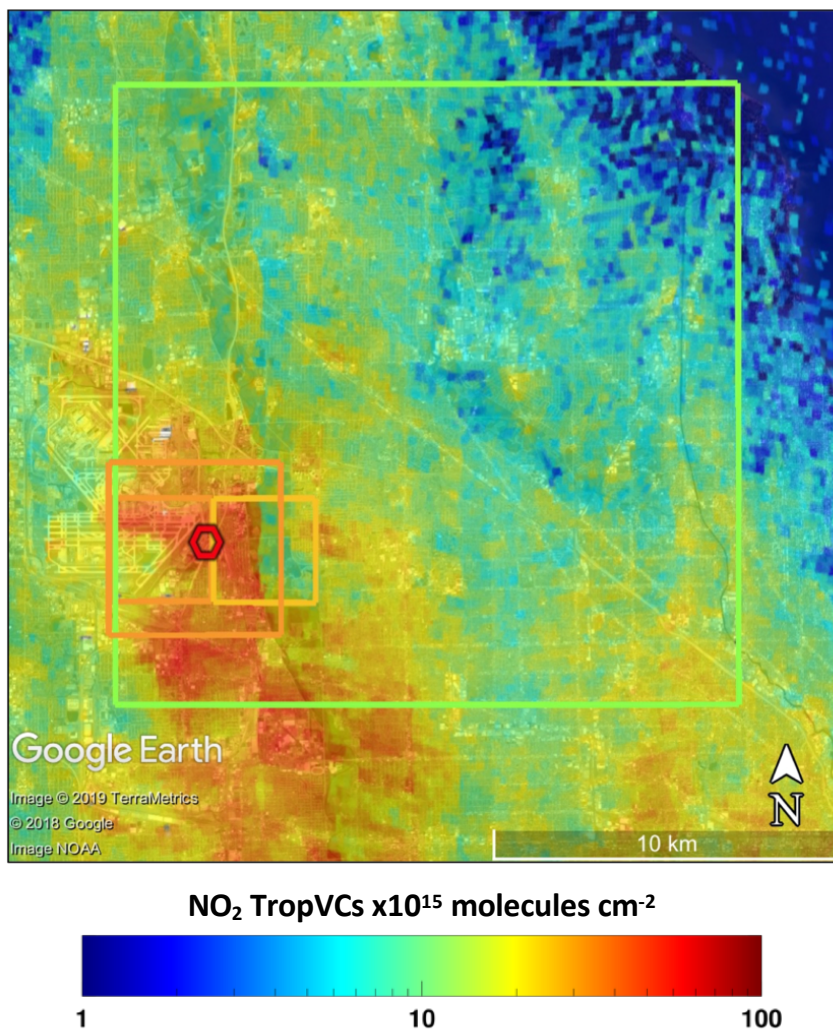
Figure 10: Map of GeoTASO TropVCs on a log10 color scale at the 250 x 250 m spatial resolution during the morning raster of June 1st, 2017 over Schiller Park (same as Figure 4) with the overlaid simulated pixels for TEMPO, TROPOMI, and OMI encompassing the Schiller Park ground site colored by the magnitude of their upscaled TropVC. The hexagon indicates the
5 **location of the Pandora and is colored by the observed NO₂ from the Pandora.**

Figure 9 illustrates that a linear relationship degrades above some threshold value of NO₂. Above the threshold, larger NO₂ values observed by Pandora are associated loss of sensitivity in NO₂ from the simulated satellite products. The threshold decreases as the resolution is coarsened. The decreasing linear slope with increasing pixel size simply results from
10 this flattening of the satellite-to-Pandora relationship at the higher NO₂ values. Such behavior makes sense if the high NO₂ values are associated with localized features rather than broad regional-scale enhancements, which is a reasonable conceptual model for urban areas such as these. The value of the threshold probably varies by region and may not be generalizable, but these results suggest that there is a limit to what magnitudes can be resolved by the spatial resolution of a particular satellite product (i.e. Pandora is only representative of each satellite product up to a certain pollution scale).
15 The data analyzed here are not sufficient to quantify thresholds, but it is possible to explore the sensitivity to different thresholds by examining how the statistics vary as the pollution threshold for Pandora coincidences is decreased.

To do this, each regression is repeated by excluding points for which Pandora TropVCs exceed 40×10^{15} molecules cm^{-2} (dashed regression line in Fig. 9) and exceed 20×10^{15} molecules cm^{-2} (solid black regression line in Fig. 9). Only the most polluted Schiller Park coincidence is excluded when filtering by Pandora TropVCs less than 40×10^{15} molecules cm^{-2}. With the removal of this point, the slopes increase (improve) and the correlations remain similar, with the exception of a notable

5   improvement at OMI resolution. The TEMPO scale comparison resembles the results at the nominal spatial scale, but slope still decreases as data are scaled to the coarser TROPOMI and OMI resolutions. Note that excluding this point slightly degrades the nominal-scale regression, demonstrating the importance of this extreme (yet valid, as shown by Fig. 4) point in a linear regression. When considering coincidences limited to Pandora TropVCs less than 20×10^{15} molecules cm^{-2}, the correlations all degrade by 5-10% due to the decreasing dynamic range with similar noise but are still on order of 0.8 or

10   better. Pixel size has less influence on calculated slope, with only a 7% decrease in slope between the nominal pixel size and the OMI scale resolutions.

This analysis shows that Pandora and satellite scale products can compare well up to the nadir pixel size of OMI for Pandora columns less than 20×10^{15} molecules cm^{-2} (though the a priori applied in this idealized satellite product is at a much finer spatial resolution than the standard satellite products). The threshold pollution scale for TROPOMI comparisons to Pandora is higher, somewhere between $20-40\times10^{15}$ molecules cm^{-2}, and for TEMPO is higher still, up to 40×10^{15} molecules

15   cm^{-2}. This analysis would benefit from more coincidences in the range of $20-60\times10^{15}$ molecules cm^{-2} to more confidently define pollution scale thresholds acceptable for Pandora and satellite product comparisons. Acceptable pollution ranges for data comparison may even vary from region-to-region as each urban area could have distinct spatial variability patterns.

These results suggest that Pandora spectrometer observations are very useful for validating satellite NO$_2$ products at

20   the spatial resolutions of TEMPO and TROPOMI, as the products are highly correlated with points tightly spanning both sides of the 1:1 line for values of up to approximately 30×10^{15} molecules cm^{-2} (and perhaps higher, but this dataset lacks sufficient observations above that level). However, even at the finest satellite product resolution (TEMPO), comparing with Pandora observations is not exempt from outliers caused by extreme degrees of subpixel heterogeneity. When choosing validation locations, areas known to have consistently strong spatiotemporal variability (e.g., Schiller Park) should be

25   avoided. When possible, additional measurements (i.e., high resolution airborne mapping) would help reduce uncertainty associated with spatial representativeness in the analysis of retrieval bias.

3.3 Comparison of OMI satellite products and ground-based Pandora measurements

During the LMOS and LA Basin flights, OMI was the highest resolution space-based platform in orbit, as TROPOMI was not launched until October of that year. Since 2004, OMI has been observing global NO$_2$ columns at city-to-regional spatial

30   scale on daily timescales. The simulated OMI comparisons in Sect. 3.2 are considered an idealized 'best case' scenario for data comparisons due to the near-nadir spatial resolution and the very high resolution a priori used for GeoTASO AMFs. In actuality, OMI's pixel area increases over 1200% from nadir to the swath edge and the a priori input for the AMF calculations have coarser spatial resolution than those used in these GeoTASO retrievals.

This section demonstrates how actual OMI observations compare with the Pandora measurements in the LMOS and

35   LA Basin domains during May-July 2017 to cover the time period in which OMI BEHR data was available while the Pandoras were operating in the two regions. Previous comparisons of OMI with Pandora column measurements in urban environments showed low to moderate correlations for vertical-to-vertical column comparisons with the biggest low biases found in areas subject to spatial heterogeneity of NO$_2$ (Lamsal et al., 2014; Reed et al., 2015; Kim et al., 2016; Goldberg et al., 2017). Improvements to the a priori input for OMI AMF calculations have been shown to help reduce biases in urban,

40   rural, and bordering transition regions (Russell et al., 2011), which is the basis of the BEHR TropVC product.

Figure 11 shows the 444 coincidences between the OMI BEHR TropVC and the Pandora TropVC (Pandora total column minus the OMI stratospheric column) with the best-fit linear regression for all points shown as a dashed black line. The points are further subset by pixel areas less than 1000 km^2 (black points and solid black regression line). Coincidence and comparison criteria are that when an OMI pixel unaffected by the row anomaly encompasses the location of a Pandora

45   with a cloud fraction less than 20%, Pandora data are averaged within a $\pm$ 5 min window of the OMI overpass time to be consistent with the temporal window used to assess variability in Sect 3.1. The horizontal whiskers show the maximum and minimum in the Pandora measurement within this 10-minute temporal window. Table 3 lists the linear regression statistics of OMI retrievals against Pandora observations for three products: the BEHR vertical column data shown in Fig. 11, the

NASA Standard Product V3 vertical column (SP TropVC), and tropospheric slant column products from OMI and Pandora (TropSC) (Recall that BEHR also uses the SP slant column). Consistently comparing these slant and vertical column statistics with respect to Pandora observations provides an assessment of the influence of AMF a priori assumptions.
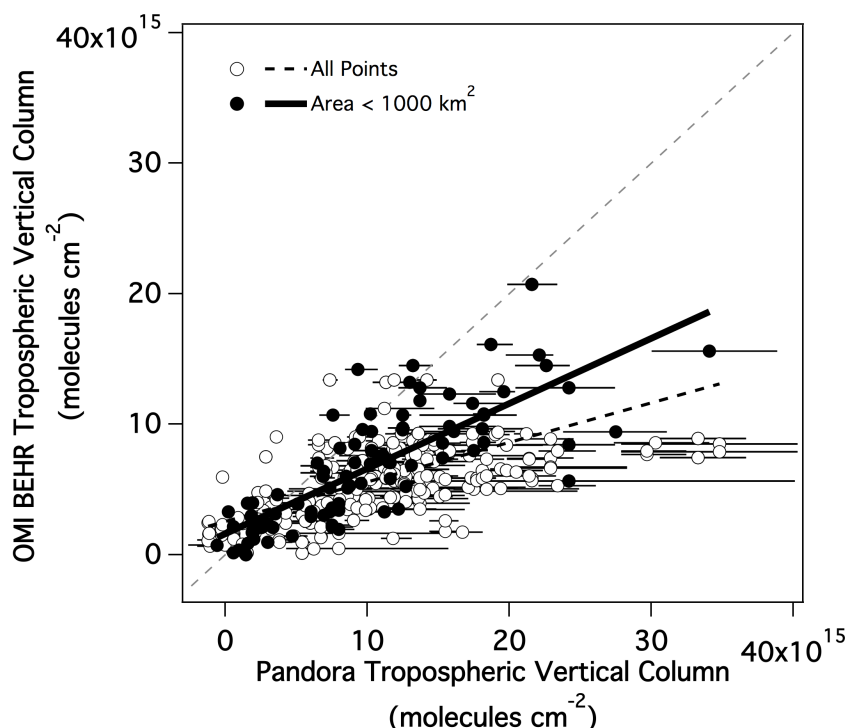
Figure 11: OMI Native Pixel BEHR NO₂ tropospheric vertical column data vs. Pandora NO₂ tropospheric column. The filled circles indicate pixel areas less than 1000 km². The linear fit to all points is shown in dashed black and the linear fit for pixels less than 1000 km² is shown in solid black. Horizontal whiskers show the maximum and minimum of Pandora data ± 5 minutes of the OMI overpass. The thin dashed line is the 1:1 line.

Considering all pixel areas, the BEHR TropVCs are moderately correlated with Pandora TropVCs but biased 50% low. The slope in this comparison is 58% percent lower than the simulated scenario discussed in Sect. 3.2. However, when only considering pixels with areas less than 1000 km², slope improves and is only 30% lower than the GeoTASO-simulated nadir OMI pixels. Restricting OMI pixels to even smaller sizes (not shown) does not result in further statistical improvement, probably because the number of coincidences quickly decreases as the areal threshold decreases (40 coincidences when including only pixel areas below 500 km² and 23 coincidences for below 400 km²). From these results, a threshold appropriate for Pandora comparisons is not clear, as deviations from the 1:1 line appear for near-nadir pixels at all pollution scales.

SP TropVCs are even 51% lower than BEHR TropVCs during all Pandora coincidences leading to a 40% lower slope for SP TropVCs and Pandora. These comparisons demonstrate the improvements due to incorporating the higher resolution a priori in the BEHR product. There is a minimal difference in r² when comparing Pandora to BEHR or SP TropVCs for OMI pixels less than 1000 km². But there is a dramatic loss in correlation between SP TropVCs and Pandora as pixel size increases, demonstrating that the impact of coarse a priori worsens with increasing pixel size.

Interestingly, OMI tropospheric slant column (TropSC) comparisons with Pandora are slightly better than SP vertical column (SP TropVC) comparisons, indicating that the SP AMF is introducing additional variance in the SP TropVC product. The loss in skill associated with applying the SP AMF is evidenced by the 30% decrease slope for all coincidences and 22% decrease for pixels less than 1000 km² in comparison to TropSC comparisons. The application of the finer-resolution BEHR AMF largely retains the amount of skill in the TropSC with a slight improvement in slope.

During LMOS/LA Basin flights, GeoTASO sampled inside 177 OMI pixels within ± 1 hour of the OMI overpass. Theoretically, satellite retrieval uncertainty could be better quantified with measurements from airborne simulators like GeoTASO that are capable of mapping entire satellite pixels. However, during these 2017 flights no OMI pixels were entirely mapped within a ± 1-hour period from the OMI overpass; the maximum OMI pixel area covered was approximately

5   80% in one coincidence and only 7 pixels were mapped by at least 50%. Therefore, GeoTASO data from these campaigns do not provide enough data to independently assess OMI uncertainty. However, with the finer spatial resolutions of new platforms (e.g. TROPOMI and TEMPO), mapping satellite pixels within an acceptable temporal threshold from the overpass time should be more easily achieved, allowing an additional point of view between the space-based observations and ground-based platforms such as Pandora.

10   **Table 3: Statistics between Pandora and OMI BEHR and SP TropVC and TropSC based on OMI pixel area.**

OMI Pixel Area	Slope			Intercept (x10^{15} molecules cm^{-2})			r^2			N
	BEHR TropVC	SP TropVC	TropSC	BEHR TropVC	SP TropVC	TropSC	BEHR TropVC	SP TropVC	TropSC	
< 1000 km^2	0.50	0.34	0.44	1.6	1.2	1.3	0.62	0.61	0.65	125
All	0.30	0.18	0.26	2.5	1.9	2.4	0.41	0.32	0.39	444

4 Conclusions

During May-June 2017, an observing strategy was executed to build a number of airborne high spatial resolution gapless maps with GeoTASO over networks of ground instruments along the western shore of Lake Michigan and in the LA Basin. Each region had a network of 5 operating Pandora spectrometers (10 total) providing accurate NO$_2$ vertical column

15   measurements at high temporal resolution with which to compare GeoTASO NO$_2$ TropVC retrievals. The sub-kilometer airborne NO$_2$ retrievals from GeoTASO are highly correlated with Pandora spectrometer observations with a slope near 1:1. Most of the apparent discrepancies between GeoTASO and Pandora TropVCs are associated with high variability and are therefore sensitive to assumptions made for identifying coincidences: e.g., the uni-directional Pandora viewing footprint vs. the omni-directional 750 m radius used to subset GeoTASO. At least one incidence of a likely GeoTASO TropVC bias

20   induced by inaccurate a priori in complex environments that are difficult to simulate (a sea breeze frontal convergence zone in this case) is shown. Despite these individual discrepancies, the GeoTASO retrievals accurately capture the spatiotemporal variability of NO$_2$ in these regions.

The raster mapping strategy at sub-kilometer resolution allows the impacts of sub-pixel heterogeneity to be assessed within the larger areal pixel resolutions of past, present, and planned satellite instruments. Data from each raster are binned

25   to a fixed grid to simulate the pixel areas of nadir observations from TEMPO (3 x 3 km), TROPOMI (5 x 5 km) and OMI (18 x 18 km). Distinct spatial features (sea breeze front, industrial areas, etc.) within urban areas of Los Angeles and Chicago can be distinguished at TEMPO, and perhaps even TROPOMI, scale but cannot be resolved at the nadir area scale of OMI. The coarseness of the OMI scale can even alias the apparent spatial location of NO$_2$ maxima within urban regions. As pixel size increases, the simulated satellite pixels lose sensitivity to the more polluted NO$_2$ plumes, leading to a degradation in the

30   linear regression with Pandora. This suggests that Pandora may only be representative of the satellite products up to a certain pollution scale and this resolvable pollution scale decreases with increasing pixel size. For OMI spatial scale, this resolvable pollution scale appears to be near 20x10^{15} molecules cm^{-2}. TROPOMI and TEMPO scale satellite products have the capability to compare well with Pandora at higher pollution scales, although more coincidences above 30x10^{15} molecules cm^{-2} would help refine this conclusion further.

Actual OMI observations show worse agreement with these Pandora data than is indicated by the idealized simulated satellite product. This is partially attributable to the decrease in OMI spatial resolution off-nadir, with some of the coincidences having pixel areas up to 1200% larger than the nadir pixel areas. When BEHR TropVC pixels are filtered to include only areas less than 1000 km^2, the Pandora linear regression slope improves by 66% and r^2 by 51%. The degraded real-world performance is also due to coarse information in the AMF calculation. An indication of this sensitivity is shown by the vertical column regression statistics against Pandora coincidences, in which the BEHR product has a better slope than the NASA Standard Product, demonstrating the benefit of higher resolution a priori inputs to the AMF calculation in the two regions of this study. Further, the regression of slant column products is actually better than the SP vertical column, showing that uncertainties introduced by coarse AMF assumptions can even degrade the satellite NO$_2$ products.

These results illustrate the past challenges in using OMI observations to evaluate the magnitude of pollution within urban areas, as the large footprint spatially averages NO$_2$ over an area that in reality has more fine-scale NO$_2$ features. With the launch of TROPOMI in October 2017 and the geostationary sensors arriving in the next decade, the unprecedented spatial and temporal resolutions offer significantly improved capability for accurately assessing pollution within urban areas. Instruments such as GeoTASO will be helpful for simulating satellite datasets over urban regions, providing a transfer standard between the satellite observations and ground-based reference measurements from validation standards such as Pandora.

Author Contributions

LMJ processed the GeoTASO NO$_2$ retrievals and led writing of the manuscript. All co-authors provided feedback on the methodology and contributed to the final manuscript. JAA, RBP, and LMJ led flight planning activities for LMOS and/or the LA Basin Flights. SJJ, MGK, and LMJ collected the GeoTASO dataset during LMOS and/or the LA Basin flights, and SJJ and MGK calibrated and processed the L1b spectra for GeoTASO. RBP provided the NAM-CMAQ analysis used in the vertical column retrieval. JJS, LCV, DW set up and monitored the Pandora spectrometers during LMOS. RS and NA provided the Pandora spectrometers for the LA Basin and NA set up the LA Basin Pandora instruments. AC, MM, and MT processed the Pandora NO$_2$ retrievals.

Data Availability

All datasets are publicly available online: GeoTASO data is archived at https://www-air.larc.nasa.gov/cgi-bin/ArcView/lmos, Pandora data are found at data.pandonia.net, and OMI data are from Laughner et al. (2018).

Acknowledgements

We would like to acknowledge NASA Earth Science Division's GEO-CAPE Mission Study for funding GeoTASO flights, the LMOS Science Teams, the South Coast Air Quality and Monitoring District (SCAQMD) and colleagues at UCLA and CalTech for providing accommodations for the Pandora instruments in the LA Basin, our EPA colleagues and site hosts for maintaining Pandora instruments in the LMOS domain, NASA SARP 2017 and NSRC, Barry Lefer and the NASA Tropospheric Composition Program for inviting us to fly as part of the Student Airborne Research Program in the LA Basin, and the NASA Langley Research Center pilots and flight crew during both field missions.

References

Beirle, S., Boersma, K. F., Platt, U., Lawrence, M. G. and Wagner, T.: Megacity Emissions and Lifetimes of Nitrogen Oxides Probed from Space, Science, 333(6050), 1737–1739, doi:10.1126/science.1207824, 2011.

Bourassa, A. E., McLinden, C. A., Sioris, C. E., Brohede, S., Bathgate, A. F., Llewellyn, E. J., and Degenstein, D. A.: Fast NO₂ retrievals from Odin-OSIRIS limb scatter measurements, Atmos. Meas. Tech., 4, 965-972, https://doi.org/10.5194/amt-4-965-2011, 2011.

5 Broccardo, S., Heue, K.-P., Walter, D., Meyer, C., Kokhanovsky, A., van der A, R., Piketh, S., Langerman, K. and Platt, U.: Intra-pixel variability in satellite tropospheric NO₂ column densities derived from simultaneous space-borne and airborne observations over the South African Highveld, Atmos. Meas. Tech., 11(5), 2797–2819, doi:10.5194/amt-11-2797-2018, 2018.

10 Bucsela, E. J., Krotkov, N. A., Celarier, E. A., Lamsal, L. N., Swartz, W. H., Bhartia, P. K., Boersma, K. F., Veefkind, J. P., Gleason, J. F. and Pickering, K. E.: A new stratospheric and tropospheric NO₂ retrieval algorithm for nadir-viewing satellite instruments: applications to OMI, Atmos. Meas. Tech., 6(10), 2607–2626, doi:10.5194/amt-6-2607-2013, 2013.

Burrows, J. P., Weber, M., Buchwitz, M., Rozanov, V., Ladstätter-Weißenmayer, A., Richter, A., DeBeek, R., Hoogen, R.,
15 Bramstedt, K. and Eichmann, K.-U.: The global ozone monitoring experiment (GOME): Mission concept and first scientific results, Journal of the Atmospheric Sciences, 56(2), 151–175, 1999.

Cede, A.: Manual for Blick Software Suite 1.3, version 7, available at: http://pandonia.net/media/documents/BlickSoftwareSuite_Manual_v7.pdf (last access: 26 March 2019), 2017.
20
CEOS: A Geostationary Satellite Constellation for Observing Global Air Quality: An International Path Forward, [online] Available from: http://ceos.org/document_management/Virtual_Constellations/ACC/Documents/AC-VC_Geostationary-Cx-for-Global-AQ-final_Apr2011.pdf (Accessed 6 March 2018), 2011.

25 EPA: Technical Note – Guidance for Developing Enhanced Monitoring Plans [online] Available from: https://www3.epa.gov/ttnamti1/files/ambient/pams/PAMS%20EMP%20Guidance.pdf (Accessed 1 April 2019).

EPA: Air Quality Statistics Report. [online] Available from: https://www.epa.gov/outdoor-air-quality-data/air-quality-statistics-report (Accessed 18 March 2019).
30
van Geffen, J. H. G., Eskes, H. J., Boersma, K. F., Maasakkers, J. D. and Veefkind, J. P.: TROPOMI ATBD of the total and tropospheric NO₂ data products, KNMI. [online] Available from: https://sentinel.esa.int/documents/247904/2476257/Sentinel-5P-TROPOMI-ATBD-NO2-data-products (Accessed 16 April 2019), 2019.

35 Goldberg, D. L., Lamsal, L. N., Loughner, C. P., Swartz, W. H., Lu, Z. and Streets, D. G.: A high-resolution and observationally constrained OMI NO₂ satellite retrieval, Atmos. Chem. Phys., 17(18), 11403–11421, doi:10.5194/acp-17-11403-2017, 2017.

Heckel, A., Kim, S.-W., Frost, G. J., Richter, A., Trainer, M. and Burrows, J. P.: Influence of low spatial resolution a priori
40 data on tropospheric NO₂ satellite retrievals, Atmos. Meas. Tech., 4(9), 1805–1820, doi:10.5194/amt-4-1805-2011, 2011.

Herman, J., Cede, A., Spinei, E., Mount, G., Tzortziou, M. and Abuhassan, N.: NO₂ column amounts from ground-based Pandora and MFDOAS spectrometers using the direct-sun DOAS technique: Intercomparisons and application to OMI validation, Journal of Geophysical Research, 114(D13), doi:10.1029/2009JD011848, 2009.
45
Herman, J., Evans, R., Cede, A., Abuhassan, N., Petropavlovskikh, I. and McConville, G.: Comparison of ozone retrievals from the Pandora spectrometer system and Dobson spectrophotometer in Boulder, Colorado, Atmospheric Measurement Techniques, 8(8), 3407–3418, doi:10.5194/amt-8-3407-2015, 2015.

IGACO: International Global Atmospheric Chemistry Observations Strategy Theme Report. (No. ESA SP-1282, GW No. 159, WMO TD No. 1235)., [online] Available from: http://www.fao.org/gtos/igos/docs/IGACO-Theme-Report-2004-4.pdf (Accessed 6 March 2018), 2004.

5 Ingmann, P., Veihelmann, B., Langen, J., Lamarre, D., Stark, H. and Courrèges-Lacoste, G. B.: Requirements for the GMES Atmosphere Service and ESA's implementation concept: Sentinels-4/-5 and -5p, Remote Sensing of Environment, 120, 58–69, doi:10.1016/j.rse.2012.01.023, 2012.

Judd, L. M., Al-Saadi, J. A., Valin, L. C., Pierce, R. B., Yang, K., Janz, S. J., Kowalewski, M. G., Szykman, J. J., 10 Tiefengraber, M. and Mueller, M.: The Dawn of Geostationary Air Quality Monitoring: Case Studies From Seoul and Los Angeles, Front. Environ. Sci., 6, doi:10.3389/fenvs.2018.00085, 2018.

Kim, H. C., Lee, P., Judd, L., Pan, L. and Lefer, B.: OMI NO_2 column densities over North American urban cities: the effect of satellite footprint resolution, Geoscientific Model Development, 9(3), 1111–1123, doi:10.5194/gmd-9-1111-2016, 2016.

15 Kim, J., Kim, M. and Choi, M.: Monitoring Aerosol Properties in East Asia from Geostationary Orbit: GOCI, MI and GEMS, in Air Pollution in Eastern Asia: An Integrated Perspective, pp. 323–333, Springer, Cham., 2017.

Krotkov, N. A., Lamsal, L. N., Celarier, E. A., Swartz, W. H., Marchenko, S. V., Bucsela, E. J., Chan, K. L., Wenig, M. and 20 Zara, M.: The version 3 OMI NO_2 standard product, Atmos. Meas. Tech., 10(9), 3133–3149, doi:10.5194/amt-10-3133-2017, 2017.

Lamsal, L. N., Krotkov, N. A., Celarier, E. A., Swartz, W. H., Pickering, K. E., Bucsela, E. J., Gleason, J. F., Martin, R. V., Philip, S., Irie, H., Cede, A., Herman, J., Weinheimer, A., Szykman, J. J. and Knepp, T. N.: Evaluation of OMI operational 25 standard NO_2 column retrievals using in situ and surface-based NO_2 observations, Atmos. Chem. Phys., 14(21), 11587–11609, doi:10.5194/acp-14-11587-2014, 2014.

Lamsal, L. N., Janz, S. J., Krotkov, N. A., Pickering, K. E., Spurr, R. J. D., Kowalewski, M. G., Loughner, C. P., Crawford, J. H., Swartz, W. H. and Herman, J. R.: High-resolution NO_2 observations from the Airborne Compact Atmospheric Mapper: 30 Retrieval and validation: High-Resolution NO_2 Observations, Journal of Geophysical Research: Atmospheres, 122(3), 1953–1970, doi:10.1002/2016JD025483, 2017.

Laughner, J., Zhu, Q., and Cohen, R.: Berkeley High Resolution (BEHR) OMI NO_2 - Native pixels, monthly profiles, UC Berkeley Dash, Dataset, https://doi.org/10.6078/D1N086, 2018.

35 Laughner, J. L., Zhu, Q., and Cohen, R. C.: Evaluation of version 3.0B of the BEHR OMI NO_2 product, Atmos. Meas. Tech., 12, 129-146, https://doi.org/10.5194/amt-12-129-2019, 2019.

Leitao, J., Richter, A., Vrekoussis, M., Kokhanovsky, A., Zhang, Q. J., Beekmann, M. and Burrows, J. P.: On the 40 improvement of NO_2 satellite retrievals – aerosol impact on the airmass factors, Atmos. Meas. Tech., 19, 2010.

Leitch, J. W., Delker, T., Good, W., Ruppert, L., Murcray, F., Chance, K., Liu, X., Nowlan, C., Janz, S. J., Krotkov, N. A., Pickering, K. E., Kowalewski, M. and Wang, J.: The GeoTASO airborne spectrometer project, edited by J. J. Butler, X. (Jack) Xiong, and X. Gu, p. 92181H., 2014.

45 Levelt, P. F., Oord, G. H. J. van den, Dobber, M. R., Malkki, A., Visser, H., Vries, J. de, Stammes, P., Lundell, J. O. V. and Saari, H.: The ozone monitoring instrument, IEEE Transactions on Geoscience and Remote Sensing, 44(5), 1093–1101, doi:10.1109/TGRS.2006.872333, 2006.

Li, J., Chen, S., Qin, W., Murefu, M., Wang, Y., Yu, Y. and Zhen, Z.: Analysis of Accuracy of MODIS BRDF Product (MCD43 C6) Based on MISR Land Surface BRF Product – A Case Study of the Central Part of Northeast Asia, ISPRS - International Archives of the Photogrammetry, Remote Sensing and Spatial Information Sciences, XLII–3, 819–823, doi:10.5194/isprs-archives-XLII-3-819-2018, 2018.

Liang, J., Horowitz, L. W., Jacob, D. J., Wang, Y., Fiore, A. M., Logan, J. A., Gardner, G. M. and Munger, J. W.: Seasonal budgets of reactive nitrogen species and ozone over the United States, and export fluxes to the global atmosphere, J. Geophys. Res., 103(D11), 13435–13450, doi:10.1029/97JD03126, 1998.

10   Liu, F., Beirle, S., Zhang, Q., Dörner, S., He, K. and Wagner, T.: NO_x lifetimes and emissions of cities and power plants in polluted background estimated by satellite observations, Atmospheric Chemistry and Physics, 16(8), 5283–5298, doi:10.5194/acp-16-5283-2016, 2016.

Liu, X., Bhartia, P. K., Chance, K., Spurr, R. J. D. and Kurosu, T. P.: Ozone profile retrievals from the Ozone Monitoring
15   Instrument, Atmos. Chem. Phys., 17, 2010.

Lucht, W., Schaaf, C. B. and Strahler, A. H.: An algorithm for the retrieval of albedo from space using semiempirical BRDF models, IEEE Transactions on Geoscience and Remote Sensing, 38(2), 977–998, doi:10.1109/36.841980, 2000.

20   McLinden, C. A., Olsen, S. C., Hannegan, B., Wild, O., Prather, M. J. and Sundet, J.: Stratospheric ozone in 3-D models: A simple chemistry and the cross-tropopause flux, Journal of Geophysical Research: Atmospheres, 105(D11), 14653–14665, doi:10.1029/2000JD900124, 2000.

Meier, A. C., Schönhardt, A., Bösch, T., Richter, A., Seyler, A., Ruhtz, T., Constantin, D.-E., Shaiganfar, R., Wagner, T.,
25   Merlaud, A., Roozendael, M. V., Belegante, L., Nicolae, D., Georgescu, L. and Burrows, J. P.: High-resolution airborne imaging DOAS measurements of NO_2 above Bucharest during AROMAT, Atmos. Meas. Tech., 27, 2017.

Noguchi, K., Richter, A., Rozanov, V., Rozanov, A., Burrows, J. P., Irie, H. and Kita, K.: Effect of surface BRDF of various land cover types on geostationary observations of tropospheric NO_2 Atmos. Meas. Tech., 7(10), 3497–3508,
30   doi:10.5194/amt-7-3497-2014, 2014.

Nowlan, C. R., Liu, X., Leitch, J. W., Chance, K., González Abad, G., Liu, C., Zoogman, P., Cole, J., Delker, T., Good, W., Murcray, F., Ruppert, L., Soo, D., Follette-Cook, M. B., Janz, S. J., Kowalewski, M. G., Loughner, C. P., Pickering, K. E., Herman, J. R., Beaver, M. R., Long, R. W., Szykman, J. J., Judd, L. M., Kelley, P., Luke, W. T., Ren, X. and Al-Saadi, J. A.:
35   Nitrogen dioxide observations from the Geostationary Trace gas and Aerosol Sensor Optimization (GeoTASO) airborne instrument: Retrieval algorithm and measurements during DISCOVER-AQ Texas 2013, Atmos. Meas. Tech., 9(6), 2647–2668, doi:10.5194/amt-9-2647-2016, 2016.

Nowlan, C. R., Liu, X., Janz, S. J., Kowalewski, M. G., Chance, K., Follette-Cook, M. B., Fried, A., González Abad, G.,
40   Herman, J. R., Judd, L. M., Kwon, H.-A., Loughner, C. P., Pickering, K. E., Richter, D., Spinei, E., Walega, J., Weibring, P., and Weinheimer, A. J.: Nitrogen dioxide and formaldehyde measurements from the GEOstationary Coastal and Air Pollution Events (GEO-CAPE) Airborne Simulator over Houston, Texas, Atmos. Meas. Tech., 11, 5941-5964, https://doi.org/10.5194/amt-11-5941-2018, 2018.

45   Palmer, P. I., Jacob, D. J., Chance, K., Martin, R. V., Spurr, R. J. D., Kurosu, T. P., Bey, I., Yantosca, R., Fiore, A. and Li, Q.: Air mass factor formulation for spectroscopic measurements from satellites: Application to formaldehyde retrievals from the Global Ozone Monitoring Experiment, J. Geophys. Res., 106(D13), 14539–14550, doi:10.1029/2000JD900772, 2001.

Pierce, R. B., T. Schaack, J. A. Al-Saadi, T. D. Fairlie, C. Kittaka, G. Lingenfelser, M. Natarajan, J. Olson, A. Soja, T.
50   Zapotocny, A. Lenzen, J. Stobie, D. Johnson, M. A. Avery, G. W. Sachse, A. Thompson, R. Cohen, J. E. Dibb, J. Crawford,

D. Rault, R. Martin, J. Szykman, and J. Fishman: Impacts of background ozone production on Houston and Dallas, Texas, air quality during the Second Texas Air Quality Study field mission, J. Geophys. Res., 114, D00F09, doi:10.1029/2008JD011337, 2009.

5   Prather, M.: Catastrophic loss of stratospheric ozone in dense volcanic clouds, Journal of Geophysical Research: Atmospheres, 97(D9), 10187–10191, doi:10.1029/92JD00845, 1992.

Reed, A. J., Thompson, A. M., Kollonige, D. E., Martins, D. K., Tzortziou, M. A., Herman, J. R., Berkoff, T. A., Abuhassan, N. K. and Cede, A.: Effects of local meteorology and aerosols on ozone and nitrogen dioxide retrievals from OMI and
10 pandora spectrometers in Maryland, USA during DISCOVER-AQ 2011, J Atmos. Chem., 72(3–4), 455–482, doi:10.1007/s10874-013-9254-9, 2015.

Russell, A. R., Perring, A. E., Valin, L. C., Bucsela, E. J., Browne, E. C., Wooldridge, P. J. and Cohen, R. C.: A high spatial resolution retrieval of NO_2 column densities from OMI: method and evaluation, Atmos. Chem. Phys., 11(16), 8543–8554,
15 doi:10.5194/acp-11-8543-2011, 2011.

C. Schaaf, Z. W.: MCD43A1 MODIS/Terra+Aqua BRDF/Albedo Model Parameters Daily L3 Global - 500m V006, doi:10.5067/modis/mcd43a1.006, 2015.

20 Spurr, R. J. D.: VLIDORT: A linearized pseudo-spherical vector discrete ordinate radiative transfer code for forward model and retrieval studies in multilayer multiple scattering media, Journal of Quantitative Spectroscopy and Radiative Transfer, 102(2), 316–342, doi:10.1016/j.jqsrt.2006.05.005, 2006.

Stajner, I., Davidson, P., Byun, D., McQueen, J., Draxler, R., Dickerson, P. and Meagher, J.: US National Air Quality
25 Forecast Capability: Expanding Coverage to Include Particulate Matter, in Air Pollution Modeling and its Application XXI, edited by D. G. Steyn and S. Trini Castelli, pp. 379–384, Springer Netherlands., 2011.

Tack, F., Merlaud, A., Meier, A. C., Vlemmix, T., Ruhtz, T., Iordache, M.-D., Ge, X., van der Wal, L., Schuettemeyer, D., Ardelean, M., Calcan, A., Constantin, D., Schönhardt, A., Meuleman, K., Richter, A. and Van Roozendael, M.:
30 Intercomparison of four airborne imaging DOAS systems for tropospheric NO_2 mapping – the AROMAPEX campaign, Atmos. Meas. Tech., 12(1), 211–236, doi:10.5194/amt-12-211-2019, 2019.

Valin, L. C., Russell, A. R., Bucsela, E. J., Veefkind, J. P., and Cohen, R. C.: Observation of slant column NO_2 using the super-zoom mode of AURA-OMI, Atmos. Meas. Tech., 4, 1929-1935, https://doi.org/10.5194/amt-4-1929-2011, 2011a.
35
Valin, L. C., Russell, A. R., Hudman, R. C., and Cohen, R. C.: Effects of model resolution on the interpretation of satellite NO_2 observations, Atmos. Chem. Phys., 11, 11647-11655, https://doi.org/10.5194/acp-11-11647-2011, 2011b.

Zoogman, P., Liu, X., Suleiman, R. M., Pennington, W. F., Flittner, D. E., Al-Saadi, J. A., Hilton, B. B., Nicks, D. K.,
40 Newchurch, M. J., Carr, J. L., Janz, S. J., Andraschko, M. R., Arola, A., Baker, B. D., Canova, B. P., Chan Miller, C., Cohen, R. C., Davis, J. E., Dussault, M. E., Edwards, D. P., Fishman, J., Ghulam, A., González Abad, G., Grutter, M., Herman, J. R., Houck, J., Jacob, D. J., Joiner, J., Kerridge, B. J., Kim, J., Krotkov, N. A., Lamsal, L., Li, C., Lindfors, A., Martin, R. V., McElroy, C. T., McLinden, C., Natraj, V., Neil, D. O., Nowlan, C. R., O'Sullivan, E. J., Palmer, P. I., Pierce, R. B., Pippin, M. R., Saiz-Lopez, A., Spurr, R. J. D., Szykman, J. J., Torres, O., Veefkind, J. P., Veihelmann, B., Wang, H.,
45 Wang, J. and Chance, K.: Tropospheric emissions: Monitoring of pollution (TEMPO), Journal of Quantitative Spectroscopy and Radiative Transfer, 186, 17–39, doi:10.1016/j.jqsrt.2016.05.008, 2017.